

AEOSR - TR - 77 - 025 5

3

Final Report

AD A 037970

The following dissertation is submitted as a
Final Report of the Josephson junction work
sponsored by Grant AFOSR 75-2867.

William O. Hamilton
Professor of Physics
Principal Investigator
February 3, 1977

Approved for public release;
distribution unlimited.

AD No. _____
DDC FILE COPY

DDC
RECEIVED
APR 8 1977
D

PII Redacted

SECURITY CLASSIFICATION OF THIS PAGE (When Data Entered)

1. REPORT DOCUMENTATION PAGE		READ INSTRUCTIONS BEFORE COMPLETING FORM	
1. REPORT NUMBER AFOSR - TR-77-0255	2. GOVT ACCESSION NO.	3. RECIPIENT'S CATALOG NUMBER 9	
4. TITLE (and Subtitle) FAR INFRARED DETECTION WITH JOSEPHSON JUNCTIONS.		5. TYPE OF REPORT & PERIOD COVERED Scientific Final rept.	
6. PERFORMING ORG. REPORT NUMBER			
7. AUTHOR(s) Chi Kong So William C. Hamilton		8. CONTRACT OR GRANT NUMBER(s) 15 VAF-AFOSR 75-2867-75	
9. PERFORMING ORGANIZATION NAME AND ADDRESS Department of Physics Louisiana State University & Agricultural & Mech. Coll. Baton Rouge LA 70803		10. PROGRAM ELEMENT, PROJECT, TASK AREA & WORK UNIT NUMBERS 16 9767-04 61102F 17	
11. CONTROLLING OFFICE NAME AND ADDRESS AFOSR/NP Bolling AFB, Bldg. #410 Wash DC 20332		12. REPORT DATE 3 Feb 1977	
14. MONITORING AGENCY NAME & ADDRESS (if different from Controlling Office) 11 Dec 76 12 102p.		13. NUMBER OF PAGES 99	
		15. SECURITY CLASS. (of this report) Unclassified	
		15a. DECLASSIFICATION/DOWNGRADING SCHEDULE	

16. DISTRIBUTION STATEMENT (of this Report)

DISTRIBUTION STATEMENT A

Approved for public release;
Distribution Unlimited

17. DISTRIBUTION STATEMENT (of the abstract entered in Block 20, if different from Report)

18. SUPPLEMENTARY NOTES

TECH OTHER

19. KEY WORDS (Continue on reverse side if necessary and identify by block number)

20. ABSTRACT (Continue on reverse side if necessary and identify by block number)

The response of Josephson junctions to microwave and far infrared radiation is studied. Junctions are formed by pressing a Nb or Nb-Ti pointed wire onto a Nb thin film which in turn is pressed against the open end of a waveguide. Electromagnetic radiation is applied through the back of the film so that only the wave magnetic field is coupled to the junction. The change of the d.c. Josephson current is monitored at different levels of microwave power over a frequency range from 22GHz to 105GHz. The dependence of the responsivity of these currents on film thickness over a range from 50 Angstroms to 500 Angstroms

is studied. The observed responsivity agrees very well with that predicted by theory. Higher responsivity is observed for thinner films and lower microwave frequencies. The observed responsivity of a 50Angstrom film junction at 22GHz is $(6 \pm 3) \times 10^{-2}$ Volt/Watt. To facilitate comparison of our results with other experiments, another coupling configuration in which the wave electric field rather than the wave magnetic field is coupled to the junction is studied. The results are comparable with other experiments. However, the responsivity in the E Vector field coupling is found to be 10(6) times more than that in the B Vector field coupling configuration. Two methods to improve the responsivity in the B Vecto field coupling configuration are suggested.

UNCLASSIFIED

Form for		
White Section	<input checked="" type="checkbox"/>	
Butt Section	<input type="checkbox"/>	
UNCLASSIFIED		
CLASSIFICATION		
BY		
DISTRIBUTION/AVAILABILITY CODES		
DISC.	AVAIL. and/or SPECIAL	
A		

FAR INFRARED DETECTION WITH
JOSEPHSON JUNCTIONS

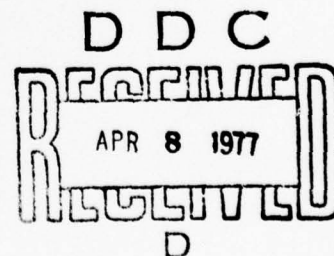
A Dissertation

Submitted to the Graduate Faculty of the
Louisiana State University and
Agricultural and Mechanical College
in partial fulfillment of the
requirements for the degree of

Doctor of Philosophy

in

The Department of Physics and Astronomy



by

Chi Kong So
B.S., The Chinese University of Hong Kong, 1970
M.S., Louisiana State University, 1972
December 1976

DISTRIBUTION STATEMENT A
Approved for public release; Distribution Unlimited

ACKNOWLEDGEMENTS

The author is indebted to Professor William O. Hamilton for his guidance, support, and encouragement during the entire course of this work.

He also wishes to express his appreciation to Dr. David G. Blair, Dr. Tom P. Bernat and Dr. Parameswaran S. Nayar for numerous advice and help.

Thanks are also due to Professor William C. Oelfke of Florida Technological University for help with the mysteries of the harmonic generator and for the loan of his equipment.

A financial assistance pertinent to the publication of this dissertation from the Dr. Charles E. Coates Memorial Fund of the LSU Foundation donated by George H. Coates is gratefully acknowledged.

This research was supported by the United States Air Force Office of Scientific Research.

TABLE OF CONTENTS

	Page
TITLE PAGE	i
ACKNOWLEDGEMENTS	ii
TABLE OF CONTENTS	iii
LIST OF TABLES	v
LIST OF FIGURES	vi
ABSTRACT	viii
 CHAPTER	
I. INTRODUCTION	1
II. THE JOSEPHSON EFFECTS AND FAR INFRARED DETECTION	4
A. The Meissner Effect and Flux Quantization	5
B. Derivation of the Basic Equations for Josephson Tunneling	11
C. The d.c. Josephson Effect	21
D. The a.c. Josephson Effect	24
E. Current-Voltage Characteristics of a Single Superconducting Point Contact	26
F. Far Infrared Detection with a Single Superconducting Point Contact	31
G. The Penetration Depth of a Superconducting Thin Film	36
III. APPARATUS AND EXPERIMENTAL PROCEDURES	40
A. Cryostat	40
B. An Electromechanical Device for Adjusting Super- Conducting Point Contact Characteristics	43

	Page
C. Sample Preparation and Electrical Connections . . .	48
D. Microwave Sources and Harmonic Generators	55
E. Measurement of Junction Voltage-Current Characteristics	62
F. Video Detection	64
IV. EXPERIMENTAL RESULTS AND DISCUSSION	68
A. \vec{B} Field Coupling Scheme	68
B. \vec{E} Field Coupling Scheme	77
V. CONCLUSION AND FUTURE EXPERIMENTS	82
REFERENCES	88
VITA	91

LIST OF TABLES

Table	Page
I. Evaporation Parameters	49
II. Typical Film Parameters	54
III. Calculated Penetration Depths	71
IV. Responsivity Versus Frequency for Various Point Contact Configurations	74

LIST OF FIGURES

Figure	Page
1. The Path of Integration Γ inside a Superconducting Cylinder	10
2. Schematic Drawing of a Josephson Junction	12
3. Integration Contour Used to Evaluate the Space Dependence of ϕ	14
4. Points P_1 and P_2 of the Barrier in the x-y Plane; Used to Evaluate Magnetic Flux	17
5. Current-Voltage Characteristics of a Single Point Contact	29
6. Equivalent Circuit Model of a Point Contact Josephson Junction	32
7. Dewar and Magnetic Shielding	41
8. Drawing of the Point Contact Adjusting Device	44
9. Relation between Junction Critical Current and Solenoid Current for a Typical Junction	47
10. Film Geometry and Electrical Connections	52
11. Block Diagrams of Microwave Systems	57
12. Chopping Circuit for Gunn Diode Oscillator	58
13. Cross Section Details of Multiplier	60
14. Block Diagram of the Biasing Circuit	63
15. Schematic Diagram of the Attenuator Network	65
16. I-V Characteristics and Voltage Response Curve of a 50 Ω Film Point Contact Junction	66
17. Schematic V-I Curve Showing how Applied Radiation Causes a Change in Zero Voltage Current which is Converted to a Voltage Output by Constant-Current External Bias	67

Figure	Page
18. Plot of Penetration Depth Versus Film Thickness . . .	72
19. Plot of Junction Responsivity at 22GHz Versus Film Thickness	75
20. Plot of Junction Responsivity at 35GHz Versus Film Thickness	76
21. Schematic Drawing of the \vec{E} Field Coupling Scheme . .	78
22. Schematic Drawing of a Double Point Contact Junction in the \vec{B} Field Coupling Scheme	83
23. Schematic Diagram of a Fabry-Perot Resonator Coupled to a Point Contact Josephson Junction . . .	86

ABSTRACT

The response of Josephson junctions to microwave and far infrared radiation is studied. Junctions are formed by pressing a Nb or Nb-Ti pointed wire onto a Nb thin film which in turn is pressed against the open end of a waveguide. Electromagnetic radiation is applied through the back of the film so that only the wave magnetic field is coupled to the junction. The change of the d.c. Josephson current is monitored at different levels of microwave power over a frequency range from 22GHz to 105GHz. The dependence of the responsivity of these currents on film thickness over a range from 50Å to 500Å is studied. The observed responsivity agrees very well with that predicted by theory. Higher responsivity is observed for thinner films and lower microwave frequencies. The observed responsivity of a 50Å film junction at 22GHz is $(6 \pm 3) \times 10^{-2}$ Volt/Watt. To facilitate comparison of our results with other experiments, another coupling configuration in which the wave electric field rather than the wave magnetic field is coupled to the junction is studied. The results are comparable with other experiments. However, the responsivity in the \vec{E} field coupling is found to be 10^6 times more than that in the \vec{B} field coupling configuration. Two methods to improve the responsivity in the \vec{B} field coupling configuration are suggested.

CHAPTER I

INTRODUCTION

In 1962 Josephson¹ predicted two remarkable phenomena occurring between two superconductors separated by a thin insulating barrier. The first one is that if the barrier is thin enough a finite current can flow across the barrier without causing a voltage to develop across the barrier. This current, called the d.c. Josephson current, depends on the phase difference between the two macroscopic quantum mechanical wavefunctions representing the states of the two superconductors and is a periodic function of the magnetic flux threading the barrier. The second phenomenon is that if a voltage difference is maintained across the barrier, an oscillating current with a frequency proportional to the voltage difference will appear across the barrier. These two phenomena are known as the d.c. and a.c. Josephson effects and any element of a device that exhibits these effects is called a Josephson junction.

One of the most promising applications of the Josephson effects is in the detection of microwave and far infrared radiation. A number of experiments²⁻⁵ have demonstrated that Josephson junctions are highly sensitive and very fast detectors in the microwave and far infrared region. Most of these experiments are performed with the junction positioned inside a waveguide or light pipe or a resonant cavity in such a way that the radiation

electric field is tightly coupled to the junction. This oscillating electric field induces a voltage across the junction which in turn modulates the d.c. Josephson current and mixes with the a.c. Josephson current by causing a phase change across the junction. This interaction results in a modification of the junction voltage-current characteristic, the change of which indicates the presence of external radiation. However, in order to calculate the junction response in this method of coupling one has to guess just what the fields are at the junction from a knowledge of the unperturbed fields because the fields at the junction are not precisely known.

In this dissertation we are performing an experiment to study the response of a point contact Josephson junction to microwave and far infrared radiation in a configuration where the electromagnetic fields at the junction are precisely known. Thus theory and experiment can be quantitatively compared. In this method of coupling a point contact is made to a thin film of a superconductor which in turn is placed across the open end of a waveguide or light pipe. Radiation is coming from the back side of the film. According to the London theory of superconductivity, the electric and magnetic fields of the radiation penetrate into a superconductor to a thickness of the order of a penetration depth. If the film is made thin enough a substantial part of the radiation magnetic field will be coupled to the junction. This high frequency magnetic field causes induced currents in the film which in turn interact with the Josephson currents resulting

in a modification of the junction voltage-current characteristic in much the same way as in the electric field coupling case. However, in this case the phase change across the junction is caused by the magnetic flux threading the junction.

In order to compare our results in this coupling scheme to the results of the other experiments^{2, 4, 5} we have also performed another experiment with the junction positioned across a waveguide so that the radiation electric field is coupled to the junction. The junction response in both coupling configurations are studied over a frequency range from 22GHz to 105GHz. The results and discussion are presented in Chapter IV of this dissertation.

In the first half of Chapter II the basic theory of the Josephson effects is discussed. In the second half of Chapter II, the basic equations for both coupling schemes are derived. Chapter III concerns with a description of the experimental techniques, sample preparation and the apparatus. In Chapter V, the final chapter, conclusion and suggestions for future experiments will be given.

CHAPTER II

THE JOSEPHSON EFFECTS AND FAR INFRARED DETECTION

In this chapter a macroscopic derivation of the Josephson equations based on phenomenological theories is given. Preceding this is a short summary of the phenomenological theory of superconductivity, containing some topics from the London⁶ and Ginzburg-Landau theory⁷, namely the Meissner effect⁶, flux quantization^{11, 12} and the derivation of the basic equations of Josephson tunneling^{7, 14}. This summary serves to facilitate the discussion of the d.c. and a.c. Josephson effects^{13, 14}.

The properties of a single superconducting point contact will be discussed in section E. Special attention will be paid to the resistive-superconductive region and the current-voltage characteristic. The point contact will be treated using a two-fluid model in which the total current is the sum of an ideal Josephson supercurrent and a normal current. The influence of a shunt capacitance and a series inductance will be taken into account.

In section F, the far infrared detection properties of a superconducting point contact will be studied in two different coupling configurations. In one only the radiation magnetic field is coupled and in the other an electric field is impressed across the junction.

Finally, section G deals with the penetration depth of a superconducting thin film in relation with its electronic mean free path. This has application to the magnetic field coupling scheme discussed in section E.

A. The Meissner Effect and Flux Quantization

According to London⁶, the essential feature of superfluidity (superconductivity) is a condensation of a macroscopic number of particles in the same single quasi-particle quantum state. Such a condensation can be usually described by an internal order parameter. The order parameter ψ_s is, according to the phenomenological theory of Ginzburg and Landau⁷, a complex quantity whose properties are similar to those of the wavefunction of the macroscopically occupied single quasi-particle quantum state. This complex order parameter ψ_s can be represented by its amplitude $\psi_0(\vec{r}, t)$ and its phase $v(\vec{r}, t)$ in the following way:

$$\psi_s = \psi_0(\vec{r}, t)e^{iv(\vec{r}, t)} \quad (1)$$

In the Ginzburg-Landau theory⁶, the square of the amplitude $|\psi_s|^2$ is interpreted as the charge density $\rho_s(T)$ of the superconducting electrons at a given temperature T , which is identical to the internal order parameter of the two fluid model of Gorter and Casimir.⁸ Hence,

$$|\psi_s|^2 = \rho_s(T) \quad (2)$$

Eq. (1) can be rewritten as

$$\psi_s = [\rho_s(\vec{r}, t)]^{1/2} e^{i\chi(\vec{r}, t)} \quad (3)$$

The absolute phase $\chi(\vec{r}, t)$ is not an observable quantity, but the gradient of the phase is as we will show later.

According to the Ginzburg-Landau theory, the current density \vec{j}_s is related to the probability current density of quantum mechanics in terms of the wavefunction ψ_s of this single quasi-particle quantum state by the following expression, which is just the current operator of elementary quantum mechanics,

$$\vec{j}_s = \frac{1}{m} \left\{ \frac{1}{2} i \hbar (\psi_s \vec{\nabla} \psi_s^* - \psi_s^* \vec{\nabla} \psi_s) - q \vec{A} |\psi_s|^2 \right\} \quad (4)$$

The charge q in Eq. (4) is equal to twice the charge of a free electron because bound electron pairs are involved in the ordering process according to the microscopic theory of Bardeen, Cooper and Schrieffer.⁹ The mass m is very nearly equal to twice the mass of a free electron.¹⁰ Substituting Eq. (3) into Eq. (4), we get

$$\vec{j}_s = |\psi_s|^2 \frac{\hbar}{m} \left[\vec{\nabla} \chi - \frac{q}{\hbar} \vec{A} \right] = |\psi_s|^2 \vec{v}_s = \rho_s \vec{v}_s \quad (5)$$

where \vec{v}_s is the velocity of the superconducting electrons. From Eq. (5) one can define the fundamental relation for the generalized dynamical momentum \vec{P}_s of the superconducting pairs

$$\vec{P}_s \equiv m \vec{v}_s + q \vec{A} = \hbar \vec{\nabla} \chi \quad (6)$$

Taking the curl of Eq. (6) the London⁶ relation is obtained

$$\vec{\nabla} \times \vec{P}_s = 0 \quad (7)$$

or

$$\vec{\nabla} \times \vec{v}_s = -\frac{q}{m} \vec{\nabla} \times \vec{A} = -\frac{q}{m} \vec{B} \quad (8)$$

Recall the Maxwell equations $\vec{\nabla} \times \vec{E} = -\frac{\partial \vec{B}}{\partial t}$ and $\vec{\nabla} \times \vec{B} = \mu_0 \vec{j}$ where the total current \vec{j} is divided into two parts: $\vec{j} = \vec{j}_s + \vec{j}_n$. The normal current, \vec{j}_n , obeys Ohm's law: $\vec{j}_n = \sigma \vec{E}$ where σ is the conductivity in the superconducting state. Combining Eq. (8) with the above equations we obtain the relationship between the total current density and the magnetic induction

$$-\vec{\nabla} \times \vec{j} = \frac{q}{m} \rho_s \vec{B} + \sigma \frac{\partial \vec{B}}{\partial t} \quad (9)$$

Eliminating \vec{j} from Eq. (9) and the first Maxwell equation listed above we obtain the following equation:

$$\vec{\nabla} \times (\vec{\nabla} \times \vec{B}) + \mu_0 \frac{q}{m} \rho_s \vec{B} + \mu_0 \sigma \frac{\partial \vec{B}}{\partial t} = 0 \quad (10)$$

Since $\vec{\nabla} \cdot \vec{B} = 0$ we can write Eq. (10) in the form:

$$\nabla^2 \vec{B} = \mu_0 \frac{q}{m} \rho_s \vec{B} + \mu_0 \sigma \frac{\partial \vec{B}}{\partial t} \quad (11)$$

Note that the two terms on the right-hand side of this equation correspond to the contributions of the supercurrent \vec{j}_s and the normal current \vec{j}_n respectively. Since $\vec{\nabla} \times \vec{j}_s = -\frac{q}{m} \rho_s \vec{B}$ and $\vec{\nabla} \times \vec{j}_n = -\sigma \frac{\partial \vec{B}}{\partial t}$, the share of each of the two currents in an alternating field of frequency $\omega/2\pi$ is given by the proportion:

$$\left| \vec{j}_s \right| : \left| \vec{j}_n \right| = 1 : \frac{\sigma \omega m}{q \rho_s}$$

For quasistationary conditions, that is, as long as ω satisfies the inequality $\omega \ll \frac{q\rho_s}{m\epsilon}$ ($\approx 10^{12} \text{ sec}^{-1}$) the normal current is negligibly small in comparison with the supercurrent.

Accordingly for quasistationary fields we have:

$$\nabla^2 \vec{B} = \frac{\vec{B}}{\lambda_L^2} \quad (12a)$$

where

$$\lambda_L^2 = \frac{m}{\mu_0 \rho_s q} \quad (12b)$$

is defined as the London penetration depth. It is shown by London⁶ that the regular solution of Eq. (12a) is satisfied by the Cartesian components of the magnetic field, i.e.,

$$\vec{B}(x) = \vec{B}(0) e^{-x/\lambda_L} \quad (13)$$

Eq. (13) accounts for the Meissner effect: the magnetic field decreases very rapidly as one recedes from the surface toward the interior of the superconductor. At a depth several times greater than λ_L , the magnetic field is practically zero. Note also the fact that even if the magnetic field was already inside the metal before cooling through the critical temperature, the magnetic field is expelled below the critical temperature.

Consider a multiple-connected superconductive region instead of a simply-connected region, for instance a superconducting cylinder whose thickness is large compared to the penetration depth. One finds that although everywhere in the superconductor $\nabla \times \vec{P}_S = 0$, the circulation of the generalized dynamical momentum

around the hole of the cylinder is quantized, $\oint_{\Gamma} P_S ds = nh$, and is also related to the magnetic flux Φ enclosed by the hole (see Fig. 1). Since the wavefunction ψ_S is single-valued at each point in the superconductor, the phase must give the same value for the wavefunction ψ_S as one goes around the cylinder and comes back to the starting point. Hence,

$$\oint_S d\varphi = 2n\pi \quad (n = \text{any integer}).$$

Inside the bulk of the superconductor $\vec{v}_S = 0$, hence Eq. (6) gives:

$$\vec{P}_S = q \vec{A} = \hbar \nabla \varphi \quad (14)$$

and the magnetic flux Φ enclosed by the hole is equal to:

$$\Phi = \iint_a B_n da = \oint_S A_S ds = \frac{1}{q} \oint_S P_S ds = \frac{\hbar}{q} \oint_S d\varphi = n \frac{h}{q} \quad (15)$$

Thus the magnetic flux trapped by a superconducting cylinder is quantized in units of h/q . The quantization of flux is first predicted in 1948 by F. London.⁶ The amount of trapped flux has been experimentally found to be quantized in units $h/2e$ by Deaver and Fairbank¹¹ and Doll and Näbauer¹² in 1961, thus verifying the BCS theory. For a closed path in a region of non-zero current ($\vec{v}_S \neq 0$) one has fluxoid quantization⁶

$$\frac{1}{q} \oint_S P_S ds = \frac{m}{q} \oint_S v_S ds + \oint_S A_S ds = \frac{m}{q} \oint_S v_S ds + \Phi = n \frac{h}{q} \quad (16)$$

It follows from Eq. (16) that if a magnetic field \vec{B} is applied through the hole (area A) of the cylinder in Fig. 1 in the normal

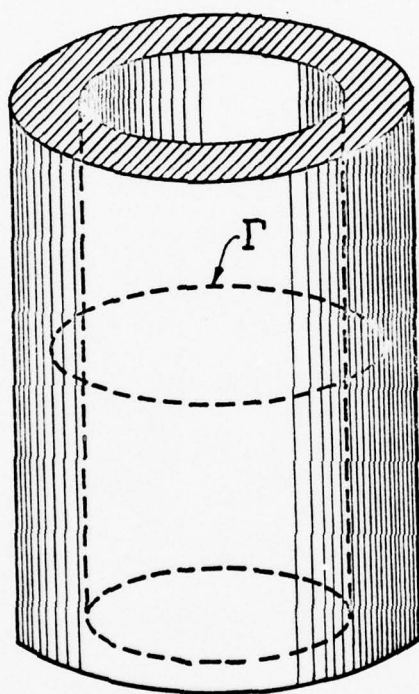


Figure 1. The path of integration Γ inside a superconducting cylinder.

state and the cylinder is subsequently cooled into the superconducting state, a persistent circulating current I_{circ} will be induced in the cylinder in such a way that the total flux enclosed by the cylinder is quantized: $BA + LI_{\text{circ}} = n (h/q)$, in which L is the self-inductance of the cylinder.

B. Derivation of the Basic Equations for Josephson Tunneling

In 1962 Josephson¹ predicted a new type of tunneling which became later known as Josephson tunneling. If two superconductors are separated from each other by a sufficiently thick barrier (insulator, semiconductor, normal metal or even a different superconductor) then the wavefunctions on the two sides are not related in any way. The phases are independent of each other. If there is no barrier at all, that is, we have one single block of superconductor, then the relative phases are fixed at each point. When the barrier is thin the wavefunctions on the two sides of the barrier are in a certain sense coupled to each other. The phenomena associated with these weakly-linked superconductors are generally referred to as the "Josephson effects."

We shall follow Solymar's¹³ approach in investigating a simple geometrical case as shown in Fig. 2 where the barrier is flat and infinitely thin. The two superconductors extend from $z = -\infty$ to 0 and from 0 to $+\infty$ respectively. The barrier lies in the $z = 0$ plane and the two sides will be referred to points at $z = +0$ and $z = -0$ respectively.

The quantities specifying the problem are as follows:

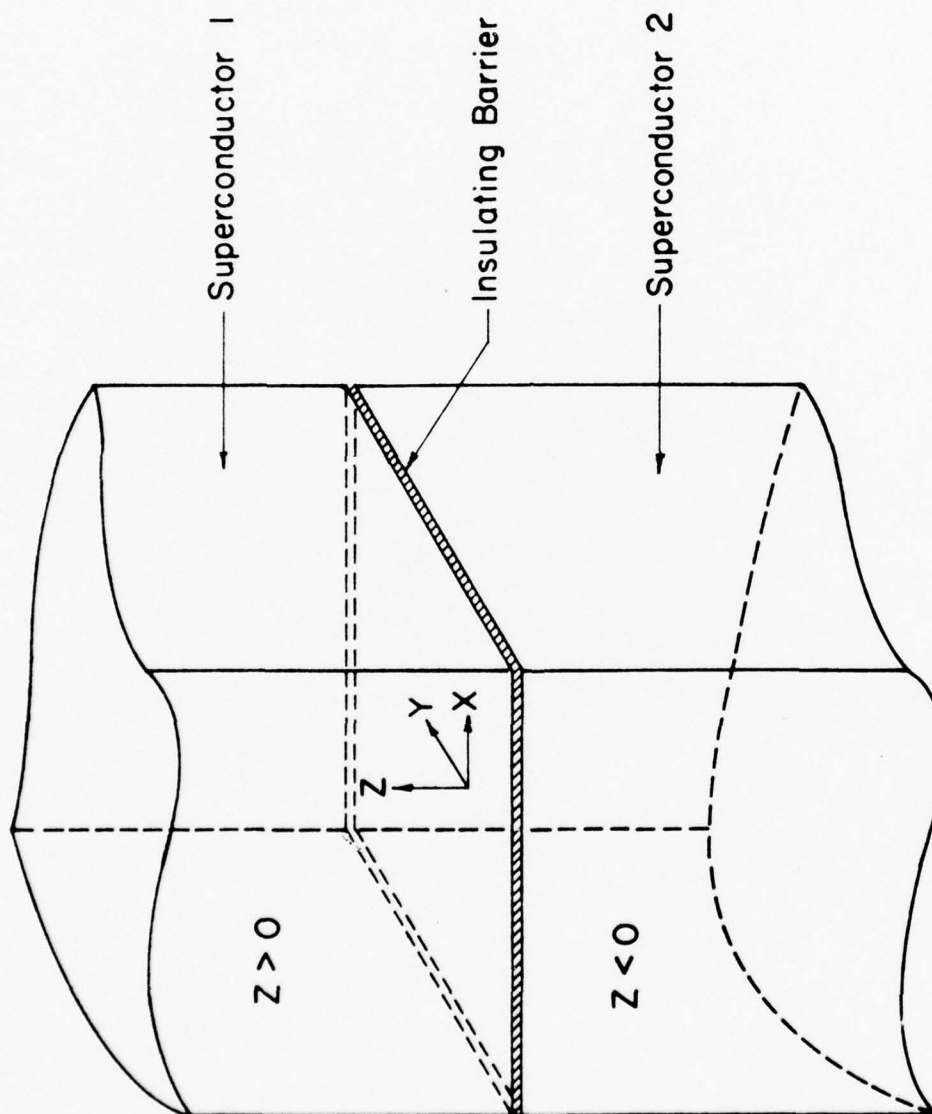


Figure 2. Schematic drawing of a Josephson Junction.

- (i) $\phi(x, y, z, t) = \psi(x, y, +0, t) - \psi(x, y, -0, t)$, the change in the phase of the wavefunction as one crosses the barrier from negative z to positive z ;
- (ii) $B_x(x, y, t)$ and $B_y(x, y, t)$ the components of the tangential magnetic field in the barrier;
- (iii) $V(x, y, t)$, the potential difference across the barrier; and
- (iv) $j_z(x, y, t)$, the current density through the barrier.

A relationship between the current density flowing in the superconductor and the gradient of the phase of the wavefunction in the presence of a magnetic field is provided by Eq. (5):

$$\nabla \psi = \frac{q}{\hbar} \left(\vec{A} + \frac{m}{q \rho_s} \vec{j}_s \right) \quad (5)$$

which is valid in the superconductor but not in the barrier. Next we need to derive an expression relating the values of ϕ at two points of the barrier, P_1 and P_2 . Denoting the coordinates of the points by $(x_1, y_1, 0)$ and $(x_2, y_2, 0)$ respectively, we may write:

$$\begin{aligned} \phi(P_1) - \phi(P_2) &= \psi(x_1, y_1, +0) - \psi(x_1, y_1, -0) - \\ &\quad \psi(x_2, y_2, +0) + \psi(x_2, y_2, -0) \end{aligned} \quad (17)$$

Integrating $\nabla \psi$ along the curves γ_- and γ_+ (Fig. 3) we get:

$$\int_{\gamma_-} \nabla \psi \cdot d\vec{s} = \psi(x_2, y_2, -0) - \psi(x_1, y_1, -0) \quad (18)$$

and

$$\int_{\gamma_+} \nabla \psi \cdot d\vec{s} = \psi(x_1, y_1, +0) - \psi(x_2, y_2, +0) \quad (19)$$

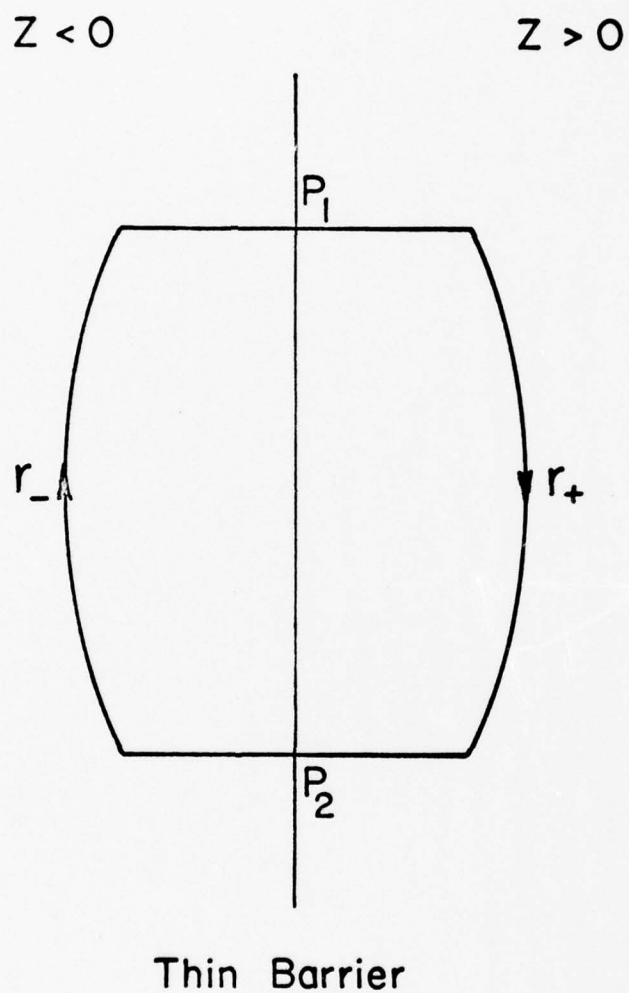


Figure 3. Integration contour used to evaluate the space dependence of ϕ .

Substituting Eqs. (18) and (19) into (17) and taking account of Eq. (5) we obtain:

$$\phi(P_1) - \phi(P_2) = \frac{q}{\hbar} \int_{\gamma_- + \gamma_+} \left(\vec{A} + \frac{m}{q \rho_s} \vec{j}_s \right) \cdot d\vec{s} \quad (20)$$

Noting that the flux quantum is $\Phi_0 = 2\pi\hbar/q$ and the line integral of the vector potential is just the magnetic flux enclosed, the first term of the integral is equal to $2\pi\Phi_r/\Phi_0$. The second term may be made arbitrarily small by choosing a suitable integration contour. This is possible because, owing to the Meissner effect, the current density declines rapidly with distance from the barrier; furthermore its direction is essentially parallel to the plane of the barrier in the penetration region. Hence the correct choice for γ is a curve which lies outside the penetration region everywhere except near P_1 and P_2 , and in the neighborhood of these points crosses the penetration region in a direction normal to the barrier as shown in Fig. 3. For such a contour Eq. (20) may be integrated to give:

$$\phi(P_1) - \phi(P_2) = 2\pi \frac{\Phi_r}{\Phi_0} \quad (21)$$

If P_1 and P_2 are close to each other we may write:

$$\Delta\phi = \frac{\partial\phi}{\partial x}\Delta x + \frac{\partial\phi}{\partial y}\Delta y \quad (22)$$

Next we derive an expression for the magnetic flux enclosed by the curve in Fig. 3. Note that the magnetic field penetrates only to a distance d which may be conveniently defined as:*

*If the thickness of the barrier is taken a finite value w then $d = w + 2\lambda$ where λ is the penetration depth of the superconductors.

$$d = \frac{1}{B(0)} \int_{-\infty}^{\infty} B(z) dz \quad (23)$$

The magnetic flux enclosed may then be obtained with the aid of Fig. 4.

$$\oint_{\mathbf{r}} = \vec{B} \cdot (\hat{i}_z \times \vec{\Delta}) d = \hat{i}_z \cdot (\vec{\Delta} \times \vec{B}) d \quad (24)$$

where: $\vec{\Delta} = \Delta x \hat{i}_x + \Delta y \hat{i}_y$ and $\hat{i}_x, \hat{i}_y, \hat{i}_z$ are unit vectors.

Eq. (24) may be reduced to the form:

$$\oint_{\mathbf{r}} = (B_y \Delta x + B_x \Delta y) d \quad (25)$$

which, compared with Eq. (21) and (22) leads to the differential equations

$$\frac{\partial \phi}{\partial x} = \frac{qd}{\hbar} B_y \quad (26)$$

$$\frac{\partial \phi}{\partial y} = - \frac{qd}{\hbar} B_x \quad (27)$$

We shall derive two more equations one relating the phase ϕ and the potential difference between the superconductors V and the other expressing the relationship between the current and the relative phase. Feynman¹⁴ obtained these two equations by extending his method of coupled modes to Josephson tunneling. According to this picture the rate of change of the wavefunction on one side depends on the actual values of the wavefunctions on both sides. The coupled differential equations are:

$$i\hbar \frac{\partial \psi_1}{\partial t} = U_1 \psi_1 + K \psi_2 \quad (28)$$

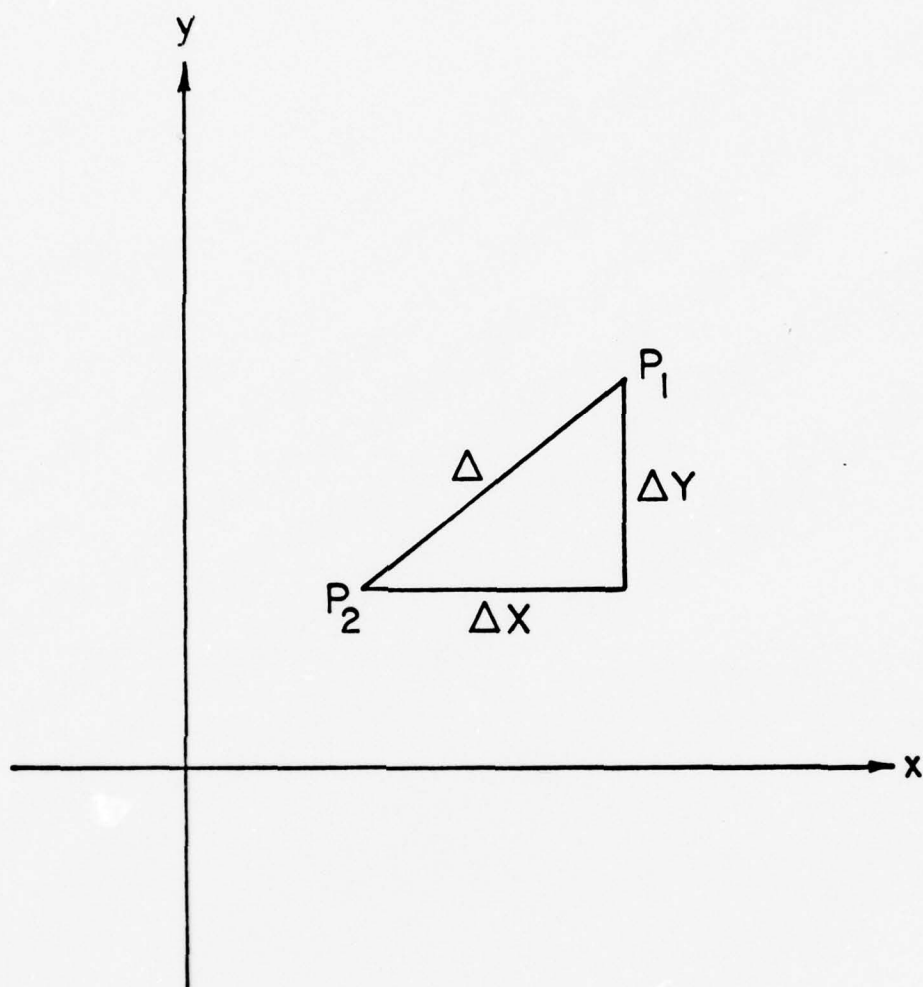


Figure 4. Points P_1 and P_2 of the barrier in the x - y plane; used to evaluate magnetic flux.

$$i\hbar \frac{\partial \psi_2}{\partial t} = U_2 \psi_2 + K \psi_1 \quad (29)$$

where U_1 and U_2 are the self energies and K is a constant characteristic of the junction. When K is zero Eqs. (28) and (29) may be solved separately; the two superconductors are independent of each other. When K is finite, the two superconductors are coupled.

In the general case when there is a voltage across the junction, the difference in self energies must be $U_1 - U_2 = qV$. We may shift then the zero of energy and rewrite Eqs. (28) and (29) as:*

$$i\hbar \frac{\partial \psi_1}{\partial t} = \frac{qV}{2} \psi_1 + K \psi_2 \quad (30)$$

$$i\hbar \frac{\partial \psi_2}{\partial t} = K \psi_1 - \frac{qV}{2} \psi_2 \quad (31)$$

Writing now both wavefunctions in the form of Eq. (3) and substituting them into Eq. (30) and (31) we get the following four differential equations:

$$\begin{aligned} \frac{\partial \rho_1}{\partial t} &= \frac{2}{\hbar} K \sqrt{\rho_1 \rho_2} \sin \phi \\ \frac{\partial \rho_2}{\partial t} &= -\frac{2}{\hbar} K \sqrt{\rho_1 \rho_2} \sin \phi \end{aligned} \quad (32)$$

$$\frac{\partial \phi}{\partial t} = -\frac{K}{\hbar} \sqrt{\frac{\rho_2}{\rho_1}} \cos \phi - \frac{qV}{2\hbar}$$

*This is for the case of no magnetic field in the junction. The generalization to include magnetic fields was done by deWaele and de Bruyn Ouboter;¹⁵ K needs then to be multiplied by an extra factor involving the integral of the vector potential across the junction.

$$\frac{\partial v_2}{\partial t} = -\frac{K}{\hbar} \sqrt{\frac{\rho_1}{\rho_2}} \cos \phi + \frac{qV}{2\hbar}$$

where we identified $v_2 - v_1$ with ϕ . Note that:

$$\frac{\partial \rho_1}{\partial t} = -\frac{\partial \rho_2}{\partial t} \quad (33)$$

that is one side loses charge at the same rate as the other side accumulates it. But whatever charge is lost it will be immediately replenished by the active element (voltage or current source) in the circuit. Taking further $\rho_1 = \rho_2 = \rho_0$ we may write for the current:

$$j_z = j_0 \sin \phi(t) \quad (34)$$

where

$$j_0 = \frac{2 K \rho_0}{\hbar} \quad (35)$$

From Eq. (32) we may also get the time dependence of ϕ :

$$\frac{\partial \phi}{\partial t} = \frac{\partial v_2}{\partial t} - \frac{\partial v_1}{\partial t} = \frac{qV}{\hbar} \quad (36)$$

The only unknown is the value of K in Eq. (35). It may be expected to depend on the properties of the superconductor on both sides of the barrier and on the thickness of the insulator. For thick barriers the coupling is small so K is small and hence the supercurrent flowing across the barrier must also be small. In fact when the barrier is thick we find no supercurrent at all. The junction exhibits only normal electron tunneling with the associated high resistance.

The magnitude of j_0 for an insulating barrier between two identical superconductors was derived from microscopic theory by Ambegaokar and Baratoff¹⁶ to be in the form:

$$j_0 = \frac{\pi \Delta(T)}{q R_{NN}} \tanh \frac{\Delta(T)}{2k T} \quad (37)$$

where R_{NN} is the resistance per unit area of the junction in the normal state and $2\Delta(T)$ is the temperature dependent energy gap of the superconductor. If the superconductors on the opposite sides of the junction are not identical j_0 must be determined by numerical methods.

We have now obtained all the necessary relations for the junction originating from the properties of the superconductors. However, Maxwell's equations are still valid in the insulator, and in the general time-dependent case a displacement current density $c_s \frac{\partial V}{\partial t}$ is present as well (where c_s is the capacitance per unit area of the junction) leading to the equation

$$\frac{\partial B_y}{\partial x} - \frac{\partial B_x}{\partial y} = \mu_0 j_z + \mu_0 c_s \frac{\partial V}{\partial t} \quad (38)$$

Eqs. (26), (27), (34), (36), and (38) now completely describe the behavior of the junction. Expressing B_y and B_x from Eqs. (26) and (27), j_z from Eq. (34), V from Eq. (36) and substituting them into Eq. (38) we obtain a single differential equation in

$$\frac{\partial^2 \phi}{\partial x^2} + \frac{\partial^2 \phi}{\partial y^2} - \frac{1}{v^2} \frac{\partial^2 \phi}{\partial t^2} = \lambda_J^{-2} \sin \phi \quad (39)$$

where:

$$\lambda_J = \left(\frac{\hbar}{\mu_0 q j_0 d} \right)^{1/2} \quad (40)$$

and

$$v = (\mu_0 c_s d)^{-1/2} \quad (41)$$

So far we have been concerned with the supercurrent only. To be more general we must add to Eq. (34) the current due to the tunneling of normal electrons as well. The complete formula derived by Josephson is of the form:

$$j_z = j_0 (V) \sin \phi + \{g_0 (V) + g_1 (V) \cos \phi\} V \quad (42)$$

in which $g_0 (V)$ and $g_1 (V) \cos \phi$ are the conductance and phase dependent conductance of the junction respectively. For most purposes $g_1 (V)$ may be neglected and $g_0 (V)$ taken as a constant. That is, Eq. (42) may be simplified to:

$$j_z = j_0 \sin \phi + g_0 V \quad (43)$$

A more general differential equation for the phase may be obtained by substituting Eq. (43) into (38) yielding

$$\left[\frac{\partial^2}{\partial x^2} + \frac{\partial^2}{\partial y^2} - \frac{1}{v^2} \frac{\partial^2}{\partial t^2} - \frac{\beta}{v^2} \frac{\partial}{\partial t} \right] \phi = \lambda_J^{-2} \sin \phi \quad (44)$$

where $\beta = g_0 / c_s$. The above differential equation has no analytical solution except in some special cases.

C. The d.c. Josephson Effect

Now let us examine the time-independent case of the four basic equations (Eqs. 26, 27, 34, and 36) derived in the last

section. From Eq. (36) it is immediately seen that $V = 0$. Furthermore, if there is no magnetic field Eqs. (26) and (27) imply that $\phi = \text{constant}$. So we are only left with Eq. (34), $j_z = j_0 \sin \phi$, which says that if $\phi \neq 0$, a supercurrent can flow through the barrier without causing a voltage drop. This is the so-called d.c. Josephson effect in zero magnetic field. It also tells us that j_0 is the maximum current density that can flow across the barrier without developing a voltage which occurs when $\phi = \pi/2$.

Next let us look at the case when there is a constant magnetic field, $\vec{B} = B_x \hat{i}_x + B_y \hat{i}_y$ in the plane of the junction. Eqs. (26) and (27) may be integrated to give

$$\phi = \frac{qd}{\hbar} (B_y x - B_x y) + \alpha \quad (45)$$

where α is an integration constant. From Eq. (45) we see that ϕ may change sign at different points of the junction. It follows from Eq. (34) that the current density may change its direction, so that the total current may become zero under certain conditions. It will soon become clear if we integrate Eq. (34) over the area of the junction giving the total current

$$\begin{aligned} I &= \int j_0 \sin \phi \, dS \\ &= \text{Im} \int j_0 \exp \left\{ i \left[\frac{qd}{\hbar} (B_y x - B_x y) + \alpha \right] \right\} dS \\ &= \text{Im} \left[e^{i\alpha} j_0 \exp \left\{ i \frac{qd}{\hbar} (B_y x - B_x y) \right\} dS \right] \end{aligned} \quad (46)$$

where Im denotes the imaginary part. It is obvious that the maximum total current occurs when this complex vector lines up

with the imaginary axis. Hence,

$$I_o = \left| \int j_o \exp \left\{ i \frac{qd}{\hbar} (B_y x - B_x y) \right\} dS \right| \quad (47)$$

Mathematically, Eq. (47) is nothing but the Fourier transform of j_o and can be evaluated if the spatial variation of j_o is known. For most cases of interest, for instance a point contact junction or a uniform junction of small area, j_o can be considered to be constant over the area of the junction. For a rectangular junction of dimensions a_x and a_y Eq. (47) reduces to:

$$I_o = I_{Jo} \left| \frac{\sin u a_x}{u a_x} \right| \left| \frac{\sin v a_y}{v a_y} \right| \quad (48)$$

where

$$u = \frac{qd}{2\hbar} B_y, \quad v = \frac{qd}{2\hbar} B_x,$$

$$\text{and } I_{Jo} = j_o a_x a_y$$

is the maximum supercurrent in the absence of a magnetic field.

In the particular case where the applied magnetic field is parallel to one of the edges of the junction (say $B_x = 0$) then we get the simple form:

$$I_o = I_{Jo} \left| \frac{\sin (\pi \Phi / \Phi_o)}{\pi \Phi / \Phi_o} \right| \quad (49)$$

where Φ denotes the magnetic flux enclosed. Thus whenever the magnetic flux is an integral multiple of Φ_o , the flux quantum, no supercurrent will flow across the junction. Anderson and Rowell¹⁷ first observed this effect in 1963. If one were to plot I_o , the maximum supercurrent, versus \vec{B} , the applied magnetic field, one would

obtain a Fraunhofer diffraction pattern with maxima and minima in I separated by a period $B_0 = \Phi_0 / da_x$.

D. The a.c. Josephson Effect

The simplest case to investigate is when a d.c. voltage V_0 appears across the junction without any applied magnetic field and the self-magnetic fields are negligible. Eqs. (26) and (27) vanish, so we are left with Eqs. (34) and (36). Integrating Eq. (36) we get:

$$\phi = \alpha + \frac{q}{\hbar} V_0 t \quad (50)$$

where α is a constant.

Substituting Eq. (50) into Eq. (34) we obtain

$$j_z = j_0 \sin \left(\alpha + \frac{q}{\hbar} V_0 t \right) \quad (51)$$

Thus we have an oscillator with oscillating frequency

$$\omega_0 = \frac{q}{\hbar} V_0 \quad (52)$$

which is proportional to the d.c. voltage.

Next let us see what happens when an a.c. voltage is applied to the junction on top of the d.c. voltage. We have

$$V = V_0 + V_1 \cos \omega t \quad (53)$$

Substituting Eq. (53) into Eq. (36) leads to

$$\dot{\phi} = \frac{q}{\hbar} V_0 t + \frac{q V_1}{\hbar \omega} \sin \omega t + \alpha \quad (54)$$

It follows from Eq. (34) that

$$j_z = j_o \sin \left\{ \frac{q}{\hbar} V_o t + \frac{qV_1}{\hbar\omega} \sin \omega t + \alpha \right\} \quad (55)$$

The above equation may be expanded into a Fourier-Bessel series¹⁸ giving

$$j_z = j_o \sum_{m=-\infty}^{\infty} J_m \left(\frac{qV_1}{\hbar\omega} \right) \sin \left\{ \left(m\omega + \frac{qV_o}{\hbar} \right) t + \alpha \right\} \quad (56)$$

where J_m is the m th order Bessel function. It may be seen that if $qV_o/\hbar\omega = n$ where n is an integer then j_z has a d.c. component

$$(j_z)_{dc} = (-1)^n j_o J_n \left(\frac{qV_1}{\hbar\omega} \right) \sin \alpha = (-1)^n j_o J_n \left(\frac{nV_1}{V_o} \right) \sin \alpha \quad (57)$$

Note that the above equation bears a lot of resemblance to Eq.

(34) of the d.c. Josephson supercurrent in the sense that in both cases the d.c. currents are determined by quantum mechanical phase differences. α is the phase difference between two oscillators with identical frequencies. One is the n th harmonic of the applied microwave radiation, the other is the Josephson frequency. When these two frequencies are locked, a d.c. current appears whose magnitude varies between $\pm I_o \left| J_n \left(\frac{qV_1}{\hbar\omega} \right) \right|$. Thus the current is in the form of a series of spikes. However, this structure has never been observed in practice. The experimentally observed I-V characteristic is considerably different. The reason for this is that the d.c. current depends on the external circuit and moreover there are other contributions to the current which have not been considered. We will take this up in the next section.

The first observation of structure in the I-V characteristics at $V_0 = n\hbar\omega/q$ was reported by Shapiro.¹⁹ The height of the current steps does follow a Bessel function dependence as it was first confirmed by Shapiro, et. al.²⁰

E. Current-Voltage Characteristics of a Single Superconducting Point Contact

One of the simplest weak connections between two superconductors is the point contact. While its inductance and capacitance are small, they may play an important role in its d.c. current-voltage characteristics. Models have been suggested to characterize its essential theoretical and experimental features. Stewart²¹ performed calculations on a single point contact shunted with a capacitance. McCumber²² calculated the I- \bar{V} characteristics of a point contact with a capacitance in parallel and also a point contact with a self-inductance in series under different circuit conditions. In this dissertation we will follow a somewhat different approach by Ouboter.¹⁵ At first both the supercurrent and the normal current through the contact will be taken into account, but the self-inductance and the capacitive coupling of the contact will be neglected. As usual, it is assumed that the linear dimensions of the contact are so small that the effect of the applied magnetic field can be neglected. The two cases for which either the current or the voltage are constants of time will be discussed. The influence of the series inductance and the shunt capacitance will be discussed at the end of the section.^{21, 22}

According to Josephson [Eqs. (34) and (36)] the super-current through a single point contact is equal to

$$I_s(t) = I_c \sin \phi(t) = I_c \sin \left\{ \phi(0) - \frac{2e}{\hbar} \int_0^t V(t') dt' \right\} \quad (58)$$

In the resistive-superconductive region $[V(t) \neq 0]$ a normal current also has to be taken into account. We will assume that this normal current is equal to $I_n(t) = \frac{V(t)}{R_n}$, where R_n is the ideal ohmic resistance of the junction. The total current is equal to

$$I(t) = I_s + I_n = I_c \sin \left\{ \phi(0) - \frac{2e}{\hbar} \int_0^t V(t') dt' \right\} + \frac{V(t)}{R_n} \quad (59)$$

First consider the case for which V is constant in time. Eq.

(59) then reduces to

$$I(t) = I_c \sin \left\{ \phi(0) - \frac{2e}{\hbar} Vt \right\} + \frac{V}{R_n} \quad (60)$$

For $V = 0$, the above expression reduces to $I = I_s = I_c \sin \phi(0)$, thus any d.c. current between $-I_c$ and $+I_c$ can flow through the junction. For $V \neq 0$, the a.c. Josephson current is sinusoidal with frequency $\nu = \frac{2e}{\hbar} V$ and amplitude I_c . The time average of $I_s(t)$ is equal to zero and only the normal component contributes to the d.c. current. The \bar{I} - V characteristic which is measured with d.c. or low-frequency methods can be described with

$$V = 0, \quad 0 \leq \overline{I(t)} \leq I_c \quad (61a)$$

$$V \neq 0, \quad \overline{I(t)} = \frac{V}{R_n} \quad (61b)$$

which is given in Fig. 5a.

Now we take $I(t)$ in Eq. (59) as a constant in time and calculate $\overline{V(t)}$. With the aid of Eq. (36) we obtain:

$$\begin{aligned} I &= I_c \sin \phi(t) + \frac{V(t)}{R_n} = I_c \sin \phi(t) + \frac{1}{R_n} \frac{\hbar}{2e} \frac{\partial \phi(t)}{\partial t} \\ &= \text{constant} \end{aligned} \quad (62)$$

When $I > I_c$, then $V(t)$ is a periodic function of $\phi(t)$ with period 2π . The voltage derived from this equation is a sharply peaked function of time, especially when I is only slightly larger than I_c .¹⁵ Furthermore, we derive from Eq. (62)

$$t = \frac{1}{R_n} \frac{\hbar}{2e} \int_{\phi(0)}^{\phi(t)} \frac{d\phi}{I - I_c \sin \phi};$$

hence

$$\frac{1}{V} = T = \frac{1}{R_n} \frac{\hbar}{2e} \int_0^{2\pi} \frac{d\phi}{I - I_c \sin \phi} \quad (63)$$

in which ν is the basic frequency of the complete signal belonging to the mean voltage $\overline{V(t)}$. The time average of the voltage is equal to the time average in one period, hence

$$\overline{V(t)} = \frac{1}{T} \int_0^T V(t) dt = \nu \frac{\hbar}{2e} \int_0^T \frac{\partial \phi}{\partial t} dt = \frac{\hbar}{2e} \nu \quad (64)$$

Substituting Eq. (63) in Eq. (64) gives

$$I > I_c; \quad \overline{V(t)} = \frac{2\pi R_n}{\int_0^{2\pi} \frac{d\phi}{I - I_c \sin \phi}} = R_n (I^2 - I_c^2)^{1/2} \quad (65a)$$

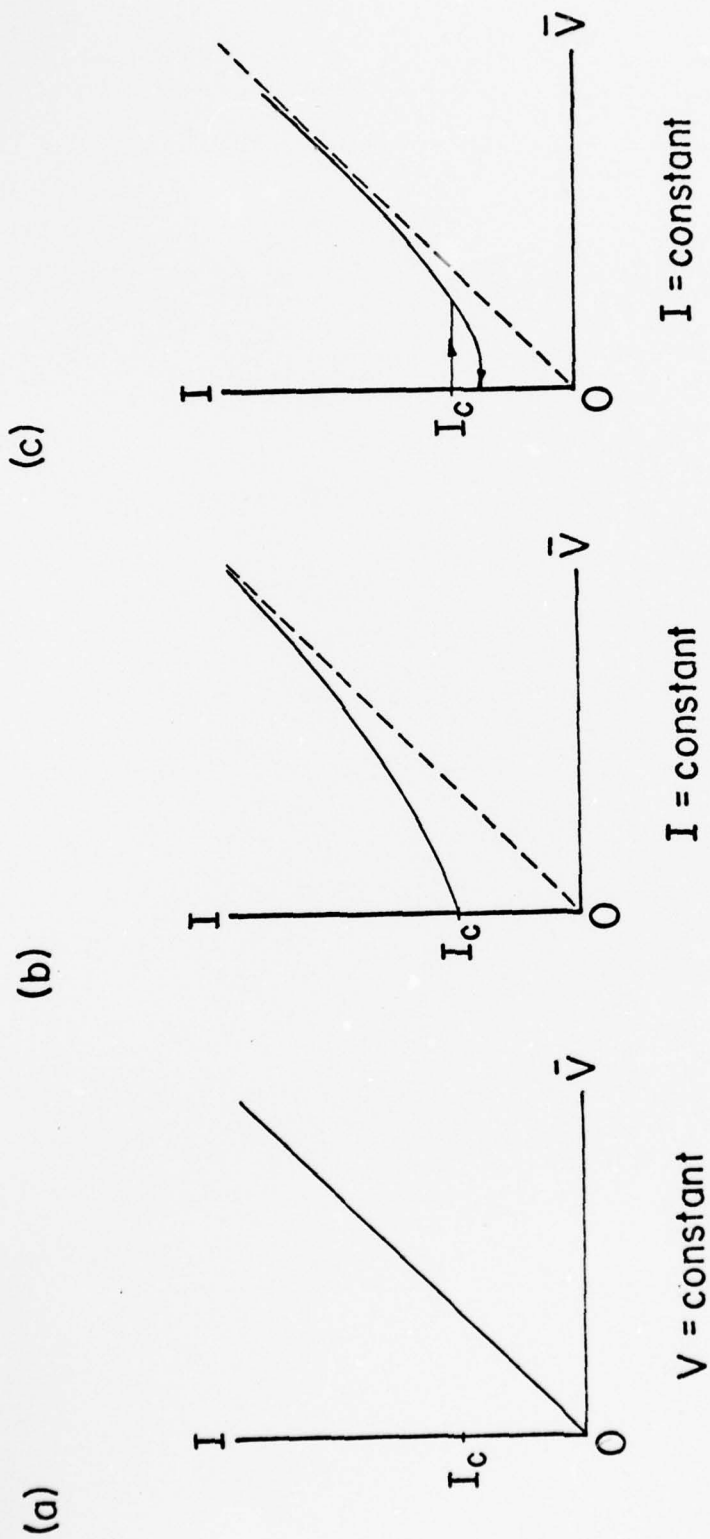


FIGURE 5

The Calculated Current-Voltage Characteristic of a Single Point Contact

- (a) When the Voltage is Constant in Time,
- (b) When the Current is Constant in Time,
- (c) When there is a Capacitance in Parallel and a Self-Inductance in Series with the Junction.

For the values of I between 0 and I_c the solution is $\phi = \text{constant}$ and consequently

$$0 \leq I \leq I_c, \quad \overline{V}(t) = 0 \quad (65b)$$

From these two equations the I - \overline{V} dependence can be calculated and is given in Fig. 5b.

Voltage biasing can be achieved by shunting the junction with a parallel ideal resistance R (where $R \ll R_n$) or an ideal capacitance C [with $1/(2\pi\nu C) \ll R_n$].^{21, 22}

A constant current can be realized experimentally if one applies the current with a circuit having high impedance. However, if one tries to measure the I - \overline{V} characteristic with such a constant-current circuit it is nearly impossible to avoid capacitive coupling between the two superconductors of order 10^{-10} pF. This capacitance does not play a significant role when $R_n \ll 1/(2\pi\nu C)$. For large values of $\overline{V}(t)$ the frequency of the a.c. currents is large and the capacitance is a short for a.c. currents between the superconductors, $R_n \gg 1/(2\pi\nu C)$. In this limit $\overline{V}(t)$ is constant in time and the I - \overline{V} characteristic approaches that of Fig. 5a. When there is also a self-inductance in series with the point contact, the I - \overline{V} dependence may be a curve as given in Fig. 5c. With a circuit having high resistance, the I - \overline{V} characteristic has an irreversible region.

Stewart²¹ and McCumber²² have performed detailed computer calculations on the system of a point contact with a capacitance C in parallel driven by a constant-current source. They both

solve the equation for the equivalent circuit shown in Fig. 6 assuming $L = 0$.

$$I = C \frac{dV(t)}{dt} + \frac{V(t)}{R_n} + I_c \sin \phi(t) = \text{constant}$$

This differential equation is analogous to that of a damped pendulum. The characteristic parameter $(\omega_J \tau)^2$ of Stewart is equal to the $\beta_c \equiv 2\pi I_c CR^2 / (\frac{h}{2e})$ of McCumber. Both predict an irreversible $I-\bar{V}$ dependence for values of $\omega_J \tau > 0.5$. For a typical point contact with $I_c = 100 \mu A$, and $R = 10$ ohms, the above condition tells us that the capacitance has to be greater than 10^{-2} pF to show this hysteresis effect. But most point contacts have capacitance of the order of 10 pF so this irreversible characteristic is very often observed.

McCumber²² also performed calculations on a point contact with a self inductance in series while the system is voltage biased. Again the $I-\bar{V}$ characteristic will become irreversible depending on a characteristic value $\beta_L \equiv (\frac{\hbar}{2e}) / (2\pi L I_c)$. Both parameters β_L and β_c are temperature dependent because I_c is temperature dependent.

F. Far Infrared Detection with a Single Superconducting Point Contact

Josephson junctions have been demonstrated to be one of the most promising, highly sensitive detectors²⁻⁵ and mixers²³ for microwave and far infrared radiation. The usual method of detection is to induce an a.c. voltage across the junction with the incident radiation. The resulting mathematical expression

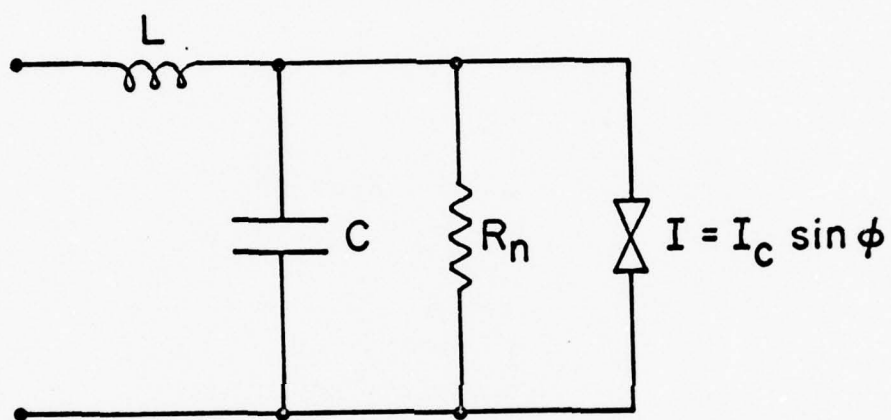


FIGURE 6

Equivalent Circuit Model of a Point Contact
Josephson Junction

for the junction critical current is obtained from Eq. (57)
by setting $n = 0$

$$I_c = I_{co} J_0 \left(\frac{q V_1}{\hbar \omega} \right) \sin \alpha \quad (66)$$

For a small high frequency signal such that $q V_1 \ll \hbar \omega$
Eq. (66) can be approximated by

$$I_c \approx I_{co} \left[1 - \left(\frac{q V_1}{2 \hbar \omega} \right)^2 \right] \quad (67)$$

in which we have set $\alpha = \pi/2$ for simplicity. Thus the resulting
change in the critical current across the junction is

$$\Delta I_c = I_{co} \left(\frac{q V_1}{2 \hbar \omega} \right)^2 \quad (68)$$

If the junction is biased at a current just larger than the
maximum critical current I_{co} , an expression for the resulting
voltage change can be obtained from Eq. (65a). However, for a
real junction the voltage change is better approximated by using
the dynamic resistance R_D of the junction at the bias point,
thus

$$\Delta \bar{V} \approx R_D \cdot \Delta I_c = I_{co} R_D \left(\frac{q V_1}{2 \hbar \omega} \right)^2 \quad (69)$$

The responsivity of the junction is defined as

$$R \equiv \frac{\Delta \bar{V}}{P} = 2 I_{co} R_D R_n \left(\frac{q}{2 \hbar \omega} \right)^2 \quad (70)$$

in which $P = V_1^2 / (2 R_n)$ is the power incident on the junction and
 R_n is the resistance of the junction in the normal state.

Most experiments so far have been done with the junction inside a waveguide, light pipe or cavity in such a way that the radiation electric field is strongly coupled to the junction. One disadvantage of this method of coupling is that the fields at the junction are not precisely known and in the cavity mode the detector is narrow banded.

In the present experiment we are measuring the response of Josephson junctions to microwave and far infrared radiation in a configuration where the fields at the junction are precisely known so that experiment and theory can be quantitatively compared. The junction is formed by pressing a pointed superconducting wire onto a superconducting thin film which in turn is placed across the open end of a waveguide or light pipe. Radiation coming from the back of the film penetrates into the film a distance of the order of a penetration depth. According to the London theory the expressions for the magnetic field and the induced current at a depth t in the film are given as:

$$B = B_0 e^{-t/\lambda} \quad (71)$$

and

$$J = \frac{B_0}{\mu_0 \lambda} e^{-t/\lambda} \quad (72)$$

in which B_0 is the amplitude of the incident magnetic field and λ is the penetration depth of the film. A method of computing λ of a thin film based on Pippard's non-local theory²⁴ will be discussed in the next section.

Now if a point contact is made to the film at a point where the induced current is high this current will cause a magnetic flux through the junction. This changing flux will modulate the d.c. Josephson current and mix with the a.c. Josephson currents by causing a phase change across the junction. The resulting mathematical expression for the d.c. Josephson current given in a previously derived equation is of the form

$$I_c = I_{co} \frac{\sin(\pi \frac{\Phi}{\Phi_0})}{\pi \frac{\Phi}{\Phi_0}} \quad (49)$$

where Φ , the magnetic flux threading the junction, is now equal to

$$\Phi = \lambda \omega B_0 e^{-t/\lambda} \quad (73)$$

in which w is the width of the junction and t is the thickness of the film.

Note that an electric field also penetrates into the film to a depth of the order of a penetration depth. But the electric field component is essentially parallel to the area of the junction and therefore does not induce a voltage across the junction as in the previous case considered. In this configuration one is effectively coupling to the radiation magnetic field rather than the electric field.

For low level radiation such that $\pi \Phi \ll \Phi_0$. Eq. (49) can be approximated by

$$I_c \approx I_{co} \left[1 - \frac{1}{6} \left(\frac{\pi \Phi}{\Phi_0} \right)^2 \right]$$

and the change in the critical current is

$$\Delta I_c = \frac{I_{co}}{6} \left(\frac{\pi \Phi}{I_o} \right)^2 \quad (74)$$

If the junction is biased at a current just larger than I_{co} the resulting voltage change is

$$\Delta \bar{V} = R_D \cdot \Delta I_c \quad (75)$$

where R_D is the dynamic resistance of the junction at the bias point. Substituting Eqs. (73), (74), and (75) into the definition of responsivity we obtain the responsivity for the magnetic field coupling scheme as

$$R \equiv \frac{\Delta \bar{V}}{P} = \frac{R_D \cdot \Delta I_c}{P} = \frac{I_{co} R_D}{6P} \left[\frac{\pi \lambda_w B_o e^{-t/\lambda}}{I_o} \right]^2. \quad (76)$$

Note that R in this case does not have the $1/\omega^2$ dependence as in the previous case considered. An expression for P in terms of B_o^2 inside a rectangular waveguide is given by Eq. (86) in Chapter IV. Substituting this equation into Eq. (76) we will obtain an expression for R independent of P and B_o^2 .

G. The Penetration Depth of a Superconducting Thin Film

In this section we will first discuss the temperature dependence of the penetration depth of a superconductor, followed by a modification of the London theory⁶ by Pippard,²⁴ and finally the form of the penetration depth for thin films.

According to the London theory⁶ the expression for the magnetic field penetration into a semi-infinite slab of superconductor has the form

$$B(x) = B_e \exp(-x/\lambda_L) \quad (77)$$

where λ_L is the London penetration depth

$$\lambda_L = (\epsilon_0 mc^2 / n_s e^2)^{1/2} \quad (78)$$

where m is the mass of an electron,

e is the charge of an electron,

and n_s is the number density of the superconducting electrons.

The only temperature-dependent factor in Eq. (78) is n_s which is assumed in the Gorter-Casimir two-fluid model⁸ to be

$$n_s(t) = (1 - t^4) n_s(0) \quad (79)$$

where $t = T/T_c$ is the reduced temperature and T_c is the transition temperature of the superconductor. Hence, the temperature dependent form of λ_L is

$$\lambda_L(t) = \lambda_L(0) / (1 - t^4)^{1/2} \quad (80)$$

The empirical temperature variation of the penetration depth is represented very closely by Eq. (80). However, the empirical values of $\lambda(0)$ turn out to be higher than what one would expect from the London definition Eq. (78), unless one makes rather unlikely assumptions of low densities of superconducting electrons or of a large effective mass. Experiments on very small samples, and measurements on impure metals, yield even higher values of $\lambda(0)$, although none of the factors in Eq. (78) appear to depend

on size or purity. This failure of the London theory will be discussed in a later section.

In 1953 Pippard measured the penetration depth in a series of dilute alloys of indium in tin, and found that the decrease in the normal electronic mean free path of the metal was accompanied by an appreciable rise in the value of $\lambda(0)$. Such a dependence of $\lambda(0)$ on the mean free path is quite incompatible with the London model, since none of the parameters in the defining Eq. (78) varies appreciably with the electronic mean free path. This experimental result, plus the above mentioned incorrectness of the London model, led Pippard²⁴ to develop a fundamental modification of this model.

Based on the concept of the range of coherence of the superconducting wave functions according to which the order parameter changes gradually over a certain distance ξ , the typical size of the Cooper pairs, Pippard proposed that λ should have the form

$$\lambda = \lambda_L \sqrt{\frac{\xi_0}{\xi(l)}} \quad (81)$$

where ξ_0 is the range of coherence of the pure superconductor ($\approx 10^{-4}$ cm) and $\xi(l)$ is an effective range of coherence of the metal depending on the mean free path l . As experimentally λ is found to increase with decreasing l , it is clear that $\xi(l)$ must decrease as l decreases. This is the result of the so-called Pippard non-local theory²⁴ which is proved by Bardeen²⁵ to be entirely equivalent to the BCS theory if one assumes:

$$\xi_0 = \hbar v_0 / \pi \Delta(0) \quad (82)$$

where $2\Delta(0)$ is the energy gap at 0°K and v_0 is the Fermi velocity at 0°K . Substituting the BCS value $2\Delta(0) = 3.52k_{\text{B}}T_{\text{c}}$ Eq. (82) becomes:

$$\xi_0 = 0.18\hbar v_0 / k_{\text{B}}T_{\text{c}} \quad (83)$$

For Nb, $v_0 = 3.4 \times 10^7$ cm/sec and $T_{\text{c}} = 9.46^\circ\text{K}$. Hence, $\xi_0 = 494 \text{ \AA}$.

For the case of small or impure specimens where the mean free path ℓ is limited by boundary as well as impurity scattering, Pippard assumes that

$$\frac{1}{\xi(\ell)} = \frac{1}{\xi_0} + \frac{1}{\alpha \ell} \quad (84)$$

where α is a constant of order unity.

From the above expression it is clear that $\xi(\ell)$ tends to ξ_0 as $\ell \rightarrow \infty$, but that $\xi(\ell) \rightarrow \ell$ as $\ell \rightarrow 0$.

Furthermore, it is now generally accepted that whenever one applies the equation of the Pippard theory to the case of small or impure specimens, one obtains good agreement by modifying Eq. (81) to²⁶

$$\lambda = \lambda_{\text{b}} \sqrt{\frac{\xi_0}{\xi(\ell)}} \quad (85)$$

where λ_{b} is now the empirical penetration depth for a bulk sample and takes the place of the London value λ_{L} .

$\lambda_{\text{b}}(0)$ for Nb is 470 \AA , as determined by Maxfield and McLean²⁷ in 1965. Hence, by Eq. (80), λ_{b} at 4.2°K is equal to 480 \AA .

CHAPTER III

APPARATUS AND EXPERIMENTAL PROCEDURES

The three independent components for this experiment consist of the following: good superconducting samples, a reliable electro-mechanical device for point contact adjustment, and a variety of microwave sources. These three are then combined in a cryostat to perform the actual experiment. Careful rf and magnetic shielding and temperature stability are required in the cryostat because of the sensitivity of the junction to magnetic fields, rf radiation, and temperature changes. The design of the cryostat is described in the next section of this chapter. This section is followed by descriptions of the point contact adjusting device, sample preparation, and the microwave system. Measurement of junction voltage-current characteristics and a video detection technique will be discussed in the last two sections of this chapter.

A. Cryostat

The cryostat and the magnetic shield arrangement are shown in Fig. 7. The final experiments are performed in a 15 cm inner diameter superinsulated metal dewar (A) with no liquid nitrogen shell. A conventional glass dewar with liquid nitrogen shell is also used in earlier experiments. The Pb plated can

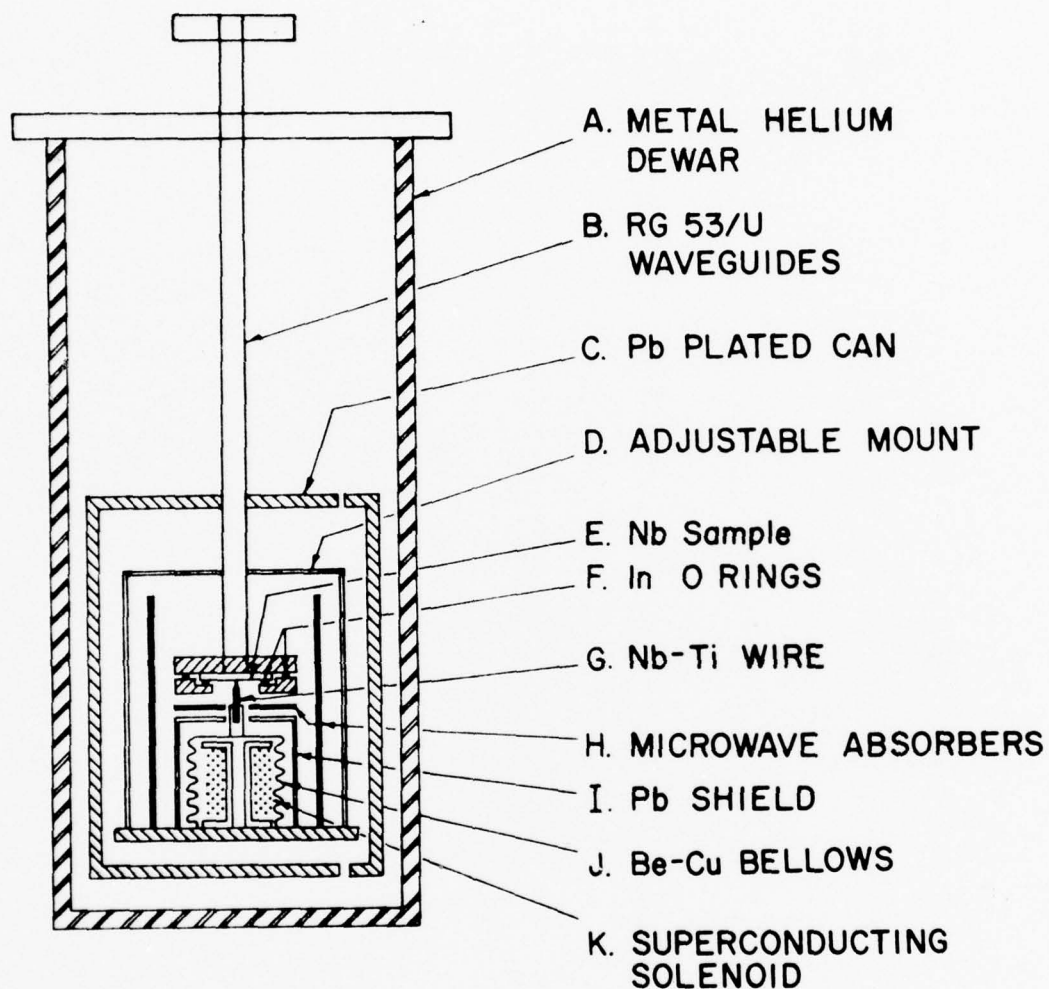


FIGURE 7

Dewar and Magnetic Shielding (Not to Scale)

(C) is fabricated by electroplating Pb on the inside and outside of a Cu can of about 9 cm outer diameter and 30 cm in length. The top of the can (C) is fastened to the waveguide (B). The room temperature end of the waveguide (B) is sealed with a mylar window. In order for the junction to be in contact with a constant temperature bath, liquid helium is allowed into the can through small holes in the top and bottom of the can.

The 19 mm diameter and .75 mm thick Nb sample (E) is mounted on the end of the waveguide (B) with a brass flange and two In o-ring seals (F). The In seals are to stop microwaves from leaking out from the sides of the substrate. To further prevent stray microwaves from reflecting back to the junction 3 mm thick nonmagnetic microwave absorbers (H) are placed between the junction and all surrounding Pb shields. The microwave absorber used is Castable Carboflow C-126 manufactured by Microwave Filter Company, Inc.

A pointed Nb-Ti wire (G) is mounted on the top plate of a soft Be-Cu bellows (J) with an insulating mount.

The Pb shield (I), the bellows (J), and the superconducting solenoid (K) are mounted on the adjustable mount (D) which is attached to the waveguide (B). The pointed Nb-Ti wire is initially separated from the Nb film by a gap of less than .7 mm. The contact is then made to the film while the apparatus is immersed in liquid helium by stretching the bellows (J) which is operated by the solenoid (K). The details of this electro-mechanical device is described in the next section.

Each of the four electrical leads into the dewar, two for the film and two for the wire, is independently shielded in a grounded 3 mm tube. To minimize rf pickup from outside the dewar, there is a commercial low-pass LC-filter in each lead.

The cryostat can be operated at any temperature between 4.2°K to 1.6°K by pumping on the liquid helium.

B. An Electromechanical Device for Adjusting Superconducting Point Contact Characteristics

The apparatus is illustrated in Fig. 8. Our junctions are formed by pressing the pointed end of a 0.6 mm diameter Nb-Ti wire onto a Nb thin film mounted at the open end of a waveguide. The desired junction V-I characteristics are obtained by varying the pressure at the points. The pointed wire is mounted upright on top of a soft bellows which is expanded by the combined magnetic repulsion of a solenoid on a superconducting plate and the attraction of the solenoid to a ferromagnetic disc. Absolute stability at the contact is achieved by putting the solenoid into a persistent mode. This kind of stability is not easily achieved with a purely mechanical design such as the commonly used differential threaded mechanism.²⁸

Referring to Fig. 8, the solenoid assembly inside the bellows consists of 1500 turns of 0.3 mm diameter Nb-Ti wire wound on a soft iron spool with a 3 mm diameter clearance hole through its axis and with a cavity at one end for a small iron disc to move up and down. An aluminum rod with one end attached

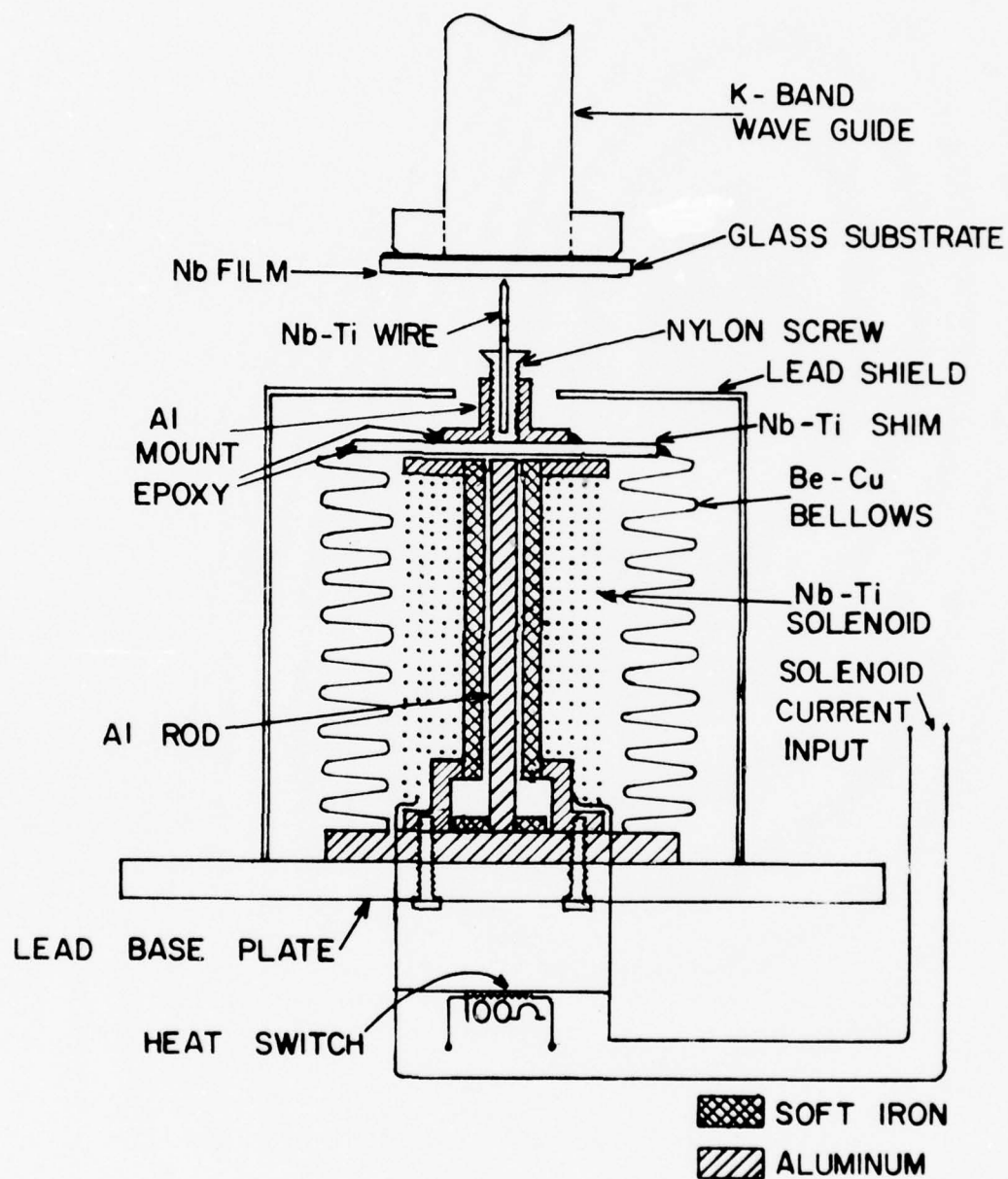


FIGURE 8

Drawing of the Point Contact Adjusting Device

to this disc is fitted loosely through the hole. The bottom of the solenoid is fixed on a base plate. The end wires of the solenoid with their copper coating taken off are joined together by spot welding to form a superconducting loop. A heat switch is put in the loop by baring about 1 cm of wire and by glueing a $1/4$ W, 100 ohm resistor around it with epoxy. It is operated at 10 V and 80 mA. Two copper wires to be used as supply leads to the solenoid are soldered to the loop at two places, one at each side of the heat switch. When the heat switch is on, this section of the loop will be driven normal and most of the current in the supply leads will flow through the solenoid. When the heat switch is off, a superconducting loop forms and the current in the solenoid will flow through the switch to form a persistent current. The L/R time constant of the solenoid is about 300 msec.

The 0.12 mm wall soft Be-Cu bellows is manufactured by Flexonics Division, Universal Oil Productions Company and has a spring constant of 1.1×10^6 dynes/cm. The dimensions of the bellows are: 3.8 cm outer diameter, 2.29 cm inner diameter, 3.43 cm length and 10 corrugations. A circular piece of 0.64 mm thick Nb-Ti sheet is glued on top of it with epoxy. The bottom of the bellows is fixed on the same base plate as that of the solenoid. When a current is passed through the solenoid, two forces combine to stretch the bellows. One is the attraction between the solenoid and the soft iron disc which pushes the rod up against the top plate. The other is the repulsion between the

magnetic field gradient of the solenoid and the superconducting top plate. With a current of 10 Å an elongation of about 3 mm is obtained.

Enclosing the bellows, at a distance of about 6 mm away on all sides, is a 0.25 mm thick lead shield. The distance is to allow the magnetic field in the solenoid to drop off so that the maximum field at the shield is less than the critical field of lead (570 oersted at 4.2°K). No magnetic disturbance is observed at the point contact as it is doubly shielded by the lead foil as well as by the Nb-Ti top plate which has a higher critical field than lead.

A typical run using this apparatus is to set the point at a distance of about 0.7 mm from the Nb film. The V-I characteristics of the junction are displayed on an oscilloscope. Initial contact can usually be made with a solenoid current of about 2 Å. The zero voltage current (d.c. Josephson current) can then be adjusted smoothly from about 40 μA to about 2 ma on a typical junction with a current increment of only 2 amperes. In Fig. 9 a plot of junction critical current vs. solenoid current for a typical run is shown. The smoothness of operation is indicative that we have a very fine linear motion at the points. The zero voltage current will remain stable, for periods of hours, once the solenoid current is put into a persistent loop. The lack of sensitivity to mechanical vibration and to small mechanical shocks is indicated by banging the dewar with the handle of a large screwdriver. No resulting change in the V-I

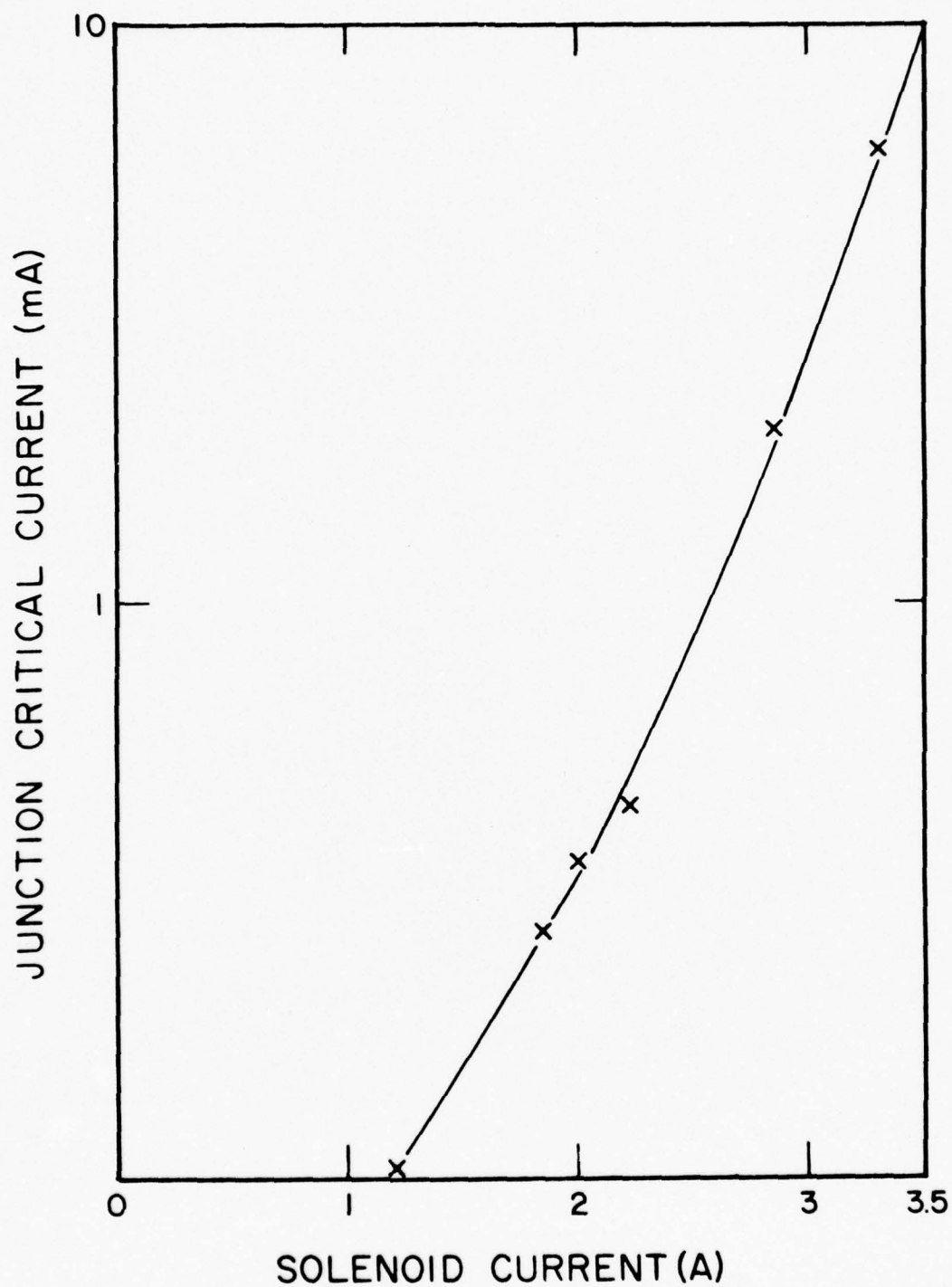


FIGURE 9

Relation between Junction Critical Current and Solenoid Current for a Typical Junction

characteristics is observed.

C. Sample Preparation and Electrical Connections

A usable sample consists of the following two parts: an evaporated superconducting film and a pointed superconducting wire. The preparation of the film is the most time consuming portion of this experiment and will be discussed next followed by the preparation of a pointed wire.

Niobium is the superconductor used for the thin film evaporation because of its high transition temperature and the hardness of the metal. Although there are a number of methods²⁹⁻³⁴ available for preparing Nb films, it appears that none has attempted films of thickness less than 100 Å. In this laboratory a successful method is developed for preparing Nb films as thin as 30 Å by electron beam evaporating Nb in a Veeco high vacuum thin film evaporator Model VE-770.

Due to the fact that there is a slow deterioration of the superconducting properties of these unprotected films, a new set of samples is required for each run. The important parameters for making the Nb films used in this experiment are given in Table I. Higher evaporation rates mean higher purity for the films. The 10 Å/sec evaporation rate for Nb is about the maximum for this particular vacuum system, probably the fault of the material. At higher evaporation rates the Nb is getting sputtered out of the crucible because the gas trapped in the molten Nb did not have a chance to escape.

TABLE I

EVAPORATION PARAMETERS

Material	Nb
Deposition Rate	Approx. 10 Å/sec
Electron Beam Power	2.5 kW
Thickness	30-1,000 Å
Substrate Material	Sapphire
Substrate Temperature	About 400°C
Evaporation Pressure	1 to 5 x 10 ⁻⁷ mmHg

The samples are prepared by electron beam evaporating Nb onto three circular and six rectangular polished sapphire substrates purchased from Adolf Meller Company. The rectangular ones of dimensions 1.27 cm x 2.54 cm and .64 mm are test samples while the circular ones of dimensions 19 mm dia. x .76 mm are used in the actual run. The Nb used is 99.99% pure and purchased from Material Research Corporation. The sapphire substrates are much better than the glass substrates used earlier in this experiment because of its much higher transmittance in the far infrared and its much higher thermal conductivity.

The substrates are first cleaned in 48% hydrofluoric acid to etch away any old Nb from previous evaporations. Secondly, they are cleaned by successively rinsing with distilled water, scrubbing with methyl alcohol, and ultrasonically cleaned in freon. The last portion of this procedure is performed in a dust free laminar flow clean bench. The substrates are mounted on a holder and put directly into the evaporator, which is then evacuated.

During evacuation a 1000 W quartz filament lamp heater mounted directly above the substrate holder is turned on. The substrate temperature is maintained at about 400°C by the heater thereafter until the evaporation is finished, which usually takes more than twelve hours. A 1.6 mm copper plate placed on top of the substrate holder is there to provide more uniform heating to all substrates. The temperature of the substrates is monitored with a copper-constantin thermocouple in contact with the substrate holder. The heating process increases adhesion of

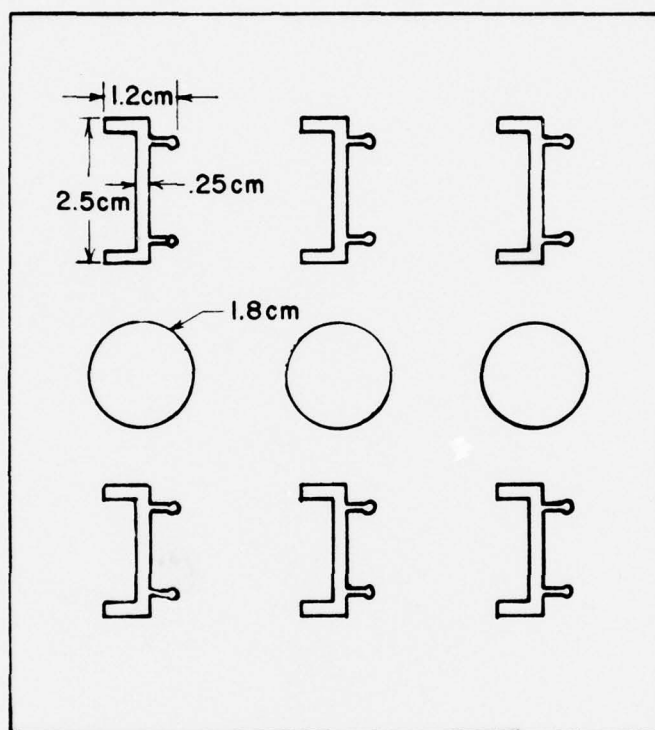
of the film to the substrates by baking out trapped gases and water molecules left on the substrates.

The bell jar is left pumping overnight with the liquid nitrogen cold trap being topped at all times with an automatic liquid nitrogen filling device. The cold trap is essential in keeping any oil vapor from getting into the bell jar. After about eight hours of pumping, baking, and cold trapping the residual pressure in the bell jar should be less than 1×10^{-7} mmHg.

Further cleaning is provided in the evaporator where the substrates are exposed to an argon glow discharge at 20-40 microns pressure for 45 min. The discharge is excited by a 10 MHz rf field of approximately 50 volts. The glow discharge cleaning process makes an obvious improvement in film quality by greatly reducing the number of pinholes.

The substrates are arranged in three columns on the substrate holder as shown in Fig. 10a. The substrates are shielded from the evaporant by a mechanical shutter. The evaporation rate is established over a period of about three hours by increasing in small increments the electron beam power from zero to 2.5 kW. During this procedure the high vacuum pressure is carefully monitored to be sure it does not exceed 5×10^{-7} mmHg. In order to guarantee the best possible film quality the deposition rate is maintained for another two hours after it has been established before depositing the films. The position of the shutter is used to control the evaporation time on each column of substrates so that three sets of films of three different

(a)



(b)

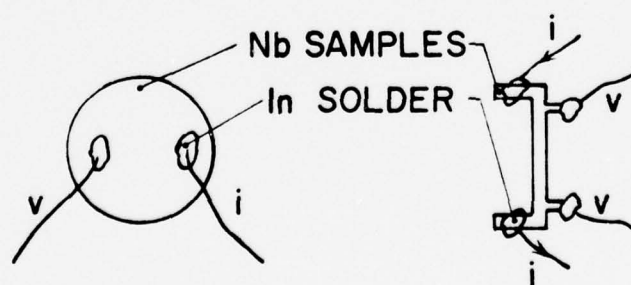


FIGURE 10

Film Geometry and Connections
 (a) Substrate Holder and Masks,
 (b) Electrical Connections

thicknesses are obtained in one evaporation.

The thickness of the sample is monitored with a Sloan thickness monitor. The output signal from the thickness monitor is proportional to the thickness of the film. An evaporation rate of about 10 \AA/sec at pressures $1-5 \times 10^{-7} \text{ mmHg}$ is found to be most satisfactory. After the film is deposited the electron beam and the quartz filament lamp are turned off and the substrates are allowed to cool to room temperature in high vacuum before removal.

Contact is made to the metal films using pure indium solder applied with an ultrasonic iron. These contacts can be recycled and do not seem to affect the quality of the films. Copper leads are soldered to the terminals of each film for current-voltage measurements as shown in Fig. 10b.

A rectangular sample is first tested in a liquid helium storage dewar for its superconducting properties. A good quality superconducting film should have a critical current density and a transition temperature close to that of the bulk material. A set of typical film parameters is shown in Table II. If the test sample is satisfactory, the circular film will be used in the actual run.

The other part of the junction is a pointed superconducting wire. In most of the runs a 0.7 mm diameter copper clad Nb-Ti wire is used. In the rest of the runs a 2.5 mm diameter pure Nb rod is used instead. The pointing procedure is the same for both wires.

After the insulation is taken off from the wire, one end

TABLE II

TYPICAL FILM PARAMETERS

Film Thickness	Resistivity Ratio $\rho_{300^{\circ}\text{K}} / \rho_{4.2^{\circ}\text{K}}$	Critical Current Density A/cm ²	Transition Temp. °K
Bulk	100	2×10^5	9.46*
500 Å	4.7	1.25×10^6	9.4
200 Å	4.6	2.5×10^6	9.3
100 Å	4.9	2.5×10^6	8.5
50 Å	4.8	1.7×10^6	7.1

*For reference see B. W. Roberts, Superconductive Materials and Some of their Properties, NBS Technical Note 408 (1966).

of it is mechanically ground to a cone shape with approximately a 40° half cone angle. This end is further chemically etched by dipping momentarily in a solution of 1:1:1 hydrofluoric acid, nitric acid, and distilled water. After rinsing in distilled water the point is examined under a 10X microscope. The tip of the cone should have a positive curvature and a diameter of about 25 microns. If this is not the case, the above process will be repeated until the desired shape of the point is obtained.

A finer point with a smaller half cone angle would seem to reduce the capacitance of the point contact and further enhance the detectivity of the junction at high frequencies. However, this is of little advantage for the present experiment because after each run the point is found to be flattened to about 100 microns in diameter for the Nb-Ti wire and about 200 microns in diameter for the Nb rod due to the hardness of the sapphire substrate.

Two copper wires are soldered to the copper clad Nb-Ti wire with Pb-Sn solder for current-voltage measurements. In the case of pure Nb contact is made to the rod by spot welding two Nb-Ti wires.

D. Microwave Sources and Harmonic Generators

Two microwave sources and two harmonic generators are used in this experiment. The combined microwave sources span a frequency range from 22 GHz to 105 GHz. It is in this frequency range that most of our data are taken.

The lower frequency source is a 50 mW Gunn effect oscillator with a center frequency at 22.125 GHz. The higher frequency source is a 200 mW OKI 35 V12 Klystron with a center frequency at 35 GHz. Two harmonic generators, both of the Gordy^{35, 36} cross waveguide type, are used to generate the third harmonics from the two fundamental sources. The details of the harmonic generators will be described below.

A block diagram of the microwave system is shown in Fig. 11. The chopping of the 22 GHz microwave is provided by an external square wave modulating the d.c. Gunn diode power supply, whereas the 35 GHz microwave is chopped by an internal square wave modulation in the Klystron power supply. The chopping circuit for the Gunn diode is shown in Fig. 12. A convenient chopping frequency for both sources is around 500 cps. The chopping of the microwaves is needed for phase sensitive detection. The output waveguides of the 35 GHz source and the two harmonic generators are coupled to the RG 53/U waveguide in the cryostat via suitable tapered transition sections.

The design of the harmonic generators is essentially the same as the one described in Gordy's paper.³⁵ Two rectangular waveguides of different sizes, one for the fundamental and the other for the third and higher harmonics, are soldered together at right angles to each other with the larger walls in contact. The contacting walls are thinned to 250 microns in order to increase the coupling between the two guides. Three holes of sizes small compared to the dimensions of the waveguides are

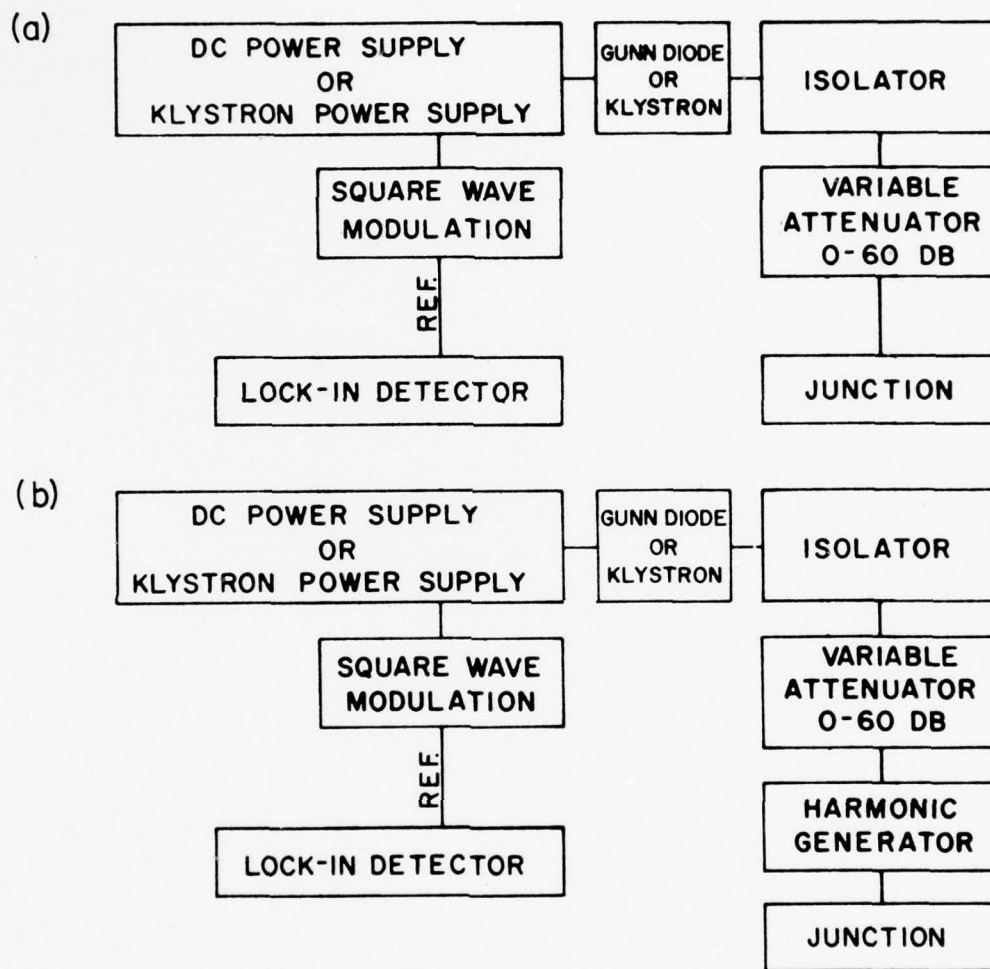


FIGURE 11

Block Diagrams of Microwave Systems

(a) 22GHz and 35GHz,

(b) 66GHz and 105GHz.

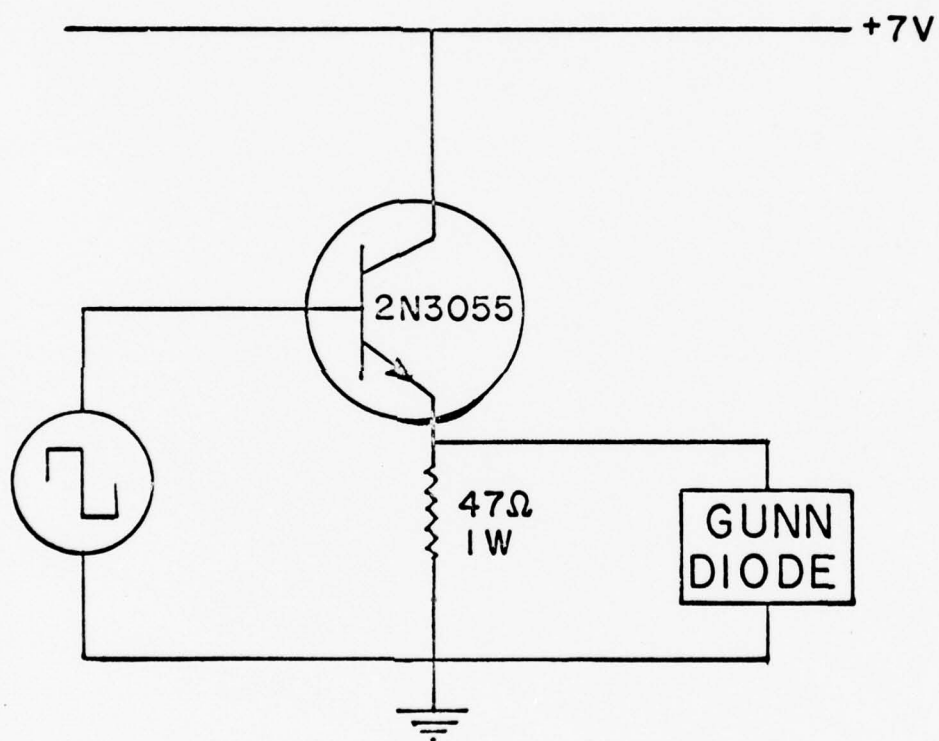


FIGURE 12

Chopping Circuit for Gunn Diode Oscillator

drilled through the walls of the cross waveguides along the axis perpendicular to and through the center of the contacting surfaces.

The harmonic generating element consists of a .5 mm x .5 mm 1N53 silicon crystal chip and a pointed 50 microns diameter tungsten cat whisker. Both the crystals and cat whisker are purchased from Alpha Industries, Inc. A cross sectional view of the multiplier is shown in Fig. 13.

The crystal is mounted on the post of a differential screw mechanism with an equivalent travel of 70 microns per revolution. The crystal is positioned at the center of the hole on the outer wall of the small waveguide. The crystal can be rotated and be screwed in and out of the hole without rotation and without touching the walls of the waveguides. This is to prevent breakage of the crystal while it is inside the hole.

The tungsten cat whisker is etched and cleaned to a smooth fine point in a solution of KOH. The etching is done by barely dipping the tip of the cat whisker in KOH and passing a small a.c. current through the cat whisker and the solution. The etching stops when the bubbling reaction at the tip of the cat whisker ceases. The cleaning is done by dipping about 0.5 cm of the cat whisker in the same KOH solution and passing a d.c. current through the cat whisker and the solution for a few seconds.

The pointed cat whisker is then examined under a microscope. The point should have a smooth cone shape with a small positive

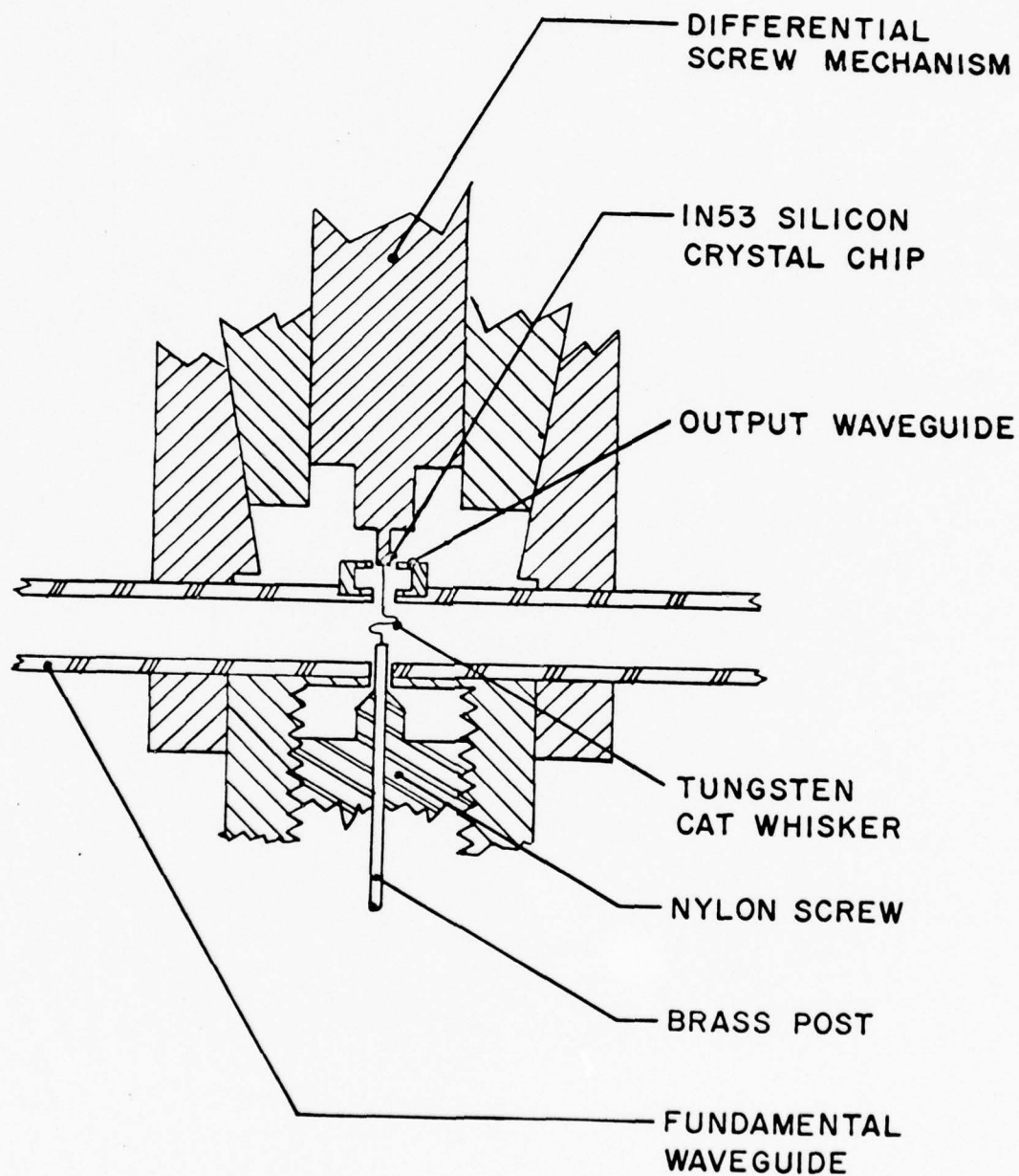


FIGURE 13

Cross Section Details of Multiplier

curvature and a fine tip. If the point is over-etched or under-etched, the above procedures are repeated with slight variations in some of the parameters until the desired point shape is obtained.

The etched and cleaned cat whisker is mounted on a nylon screw and then threaded through the holes in the cross waveguides until it reaches the inner surface of the outer hole in the small waveguide. The bend in the cat whisker provides more strength to the point contact and also acts as a partial choke to the harmonics generated in the small waveguide.

When mounting the differential screw mechanism onto the cross waveguides it is best to back off the crystal far enough so that it ends up just outside the outer hole in the small waveguide. The crystal is then advanced slowly through the hole until contact is made to the cat whisker.

The condition of the contact is monitored with a sensitive ammeter. The moment the cat whisker touches the crystal, a microwave induced current will show up in the ammeter. In case the cat whisker hits the post or the walls of the waveguides instead of the crystal a current in the opposite direction will result. The best contact is usually the first contact with the lightest pressure and maximum induced current in the diode. After a few trials the cat whisker will become blunt and it has to be etched and cleaned again.

The harmonic output is tuned to maximum with the two shorting plungers at one of the ends of each cross waveguide. The output power is further optimized by reverse biasing the

diode at a voltage slightly less than its breakdown voltage. The output power is estimated to within ± 5 dB by detecting with a 1N53 diode commercial crystal detector. The 1N53 diode is calibrated against the known output powers from the fundamentals.

The performance of the harmonic generators depends on the cleanliness of the crystal and cat whisker contact. If the performance of the generator is degraded, the cat whisker has to be recleaned and/or re-etched in a KOH solution. The average conversion loss of the 66 GHz harmonic is about 40 dB whereas that of the 105 GHz harmonic is about 30 dB.

The reason why there is more loss at 66 GHz than at 105 GHz is because the crystals in the two harmonic generators are different. The 66 GHz harmonic generator employed silicon crystal material from cartridge-mounted 1N53 diodes. However, at a later stage of this experiment we were fortunate to have on loan a 105 GHz harmonic generator and a 200 mW V-band source from Professor W. C. Oelfke of Florida Technological University. The crystal employed in this multiplier is an improved silicon crystal bombarded with high energy radiation obtained from Bell Telephone Laboratories. These crystals were found to improve the performance of the multiplier unit. The method of development of this crystal is described by Ohl, Budenstein, and Burrus³⁷ of the Bell Telephone Laboratories.

E. Measurement of Junction Voltage-Current Characteristics (VICs)

A block diagram of the biasing circuit is shown in Fig. 14. The triangle wave generator and the d.c. amplifier are built

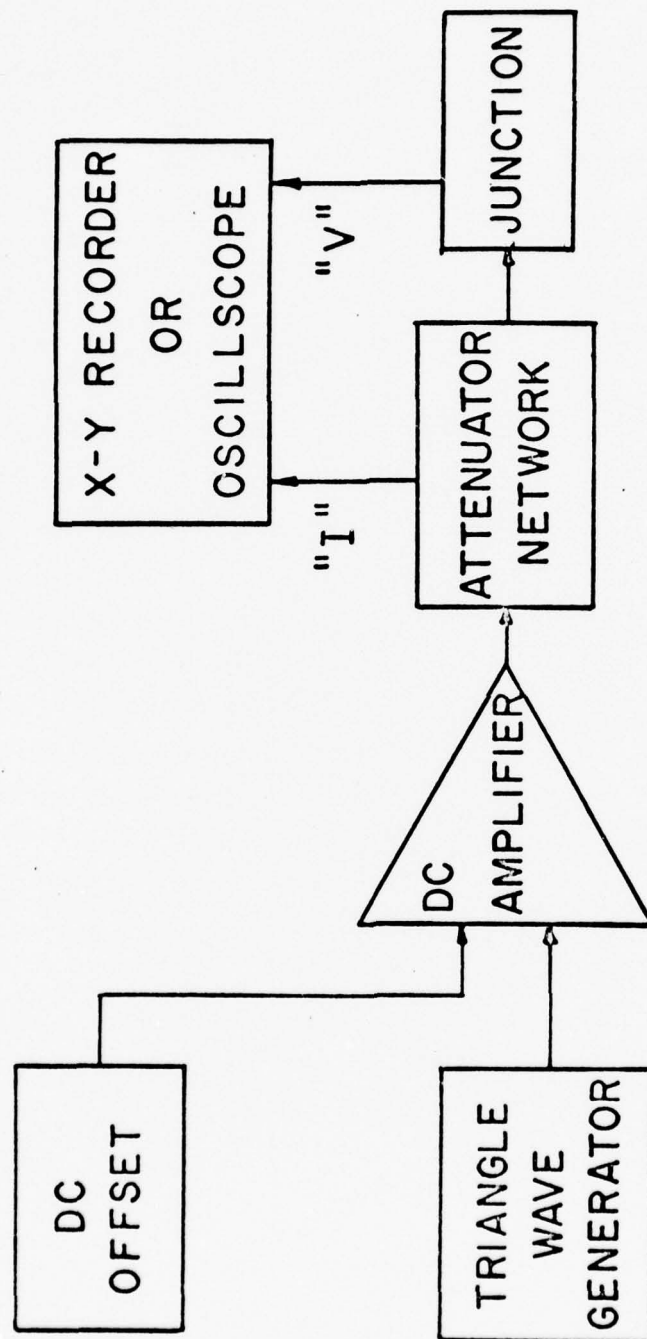


FIGURE 14

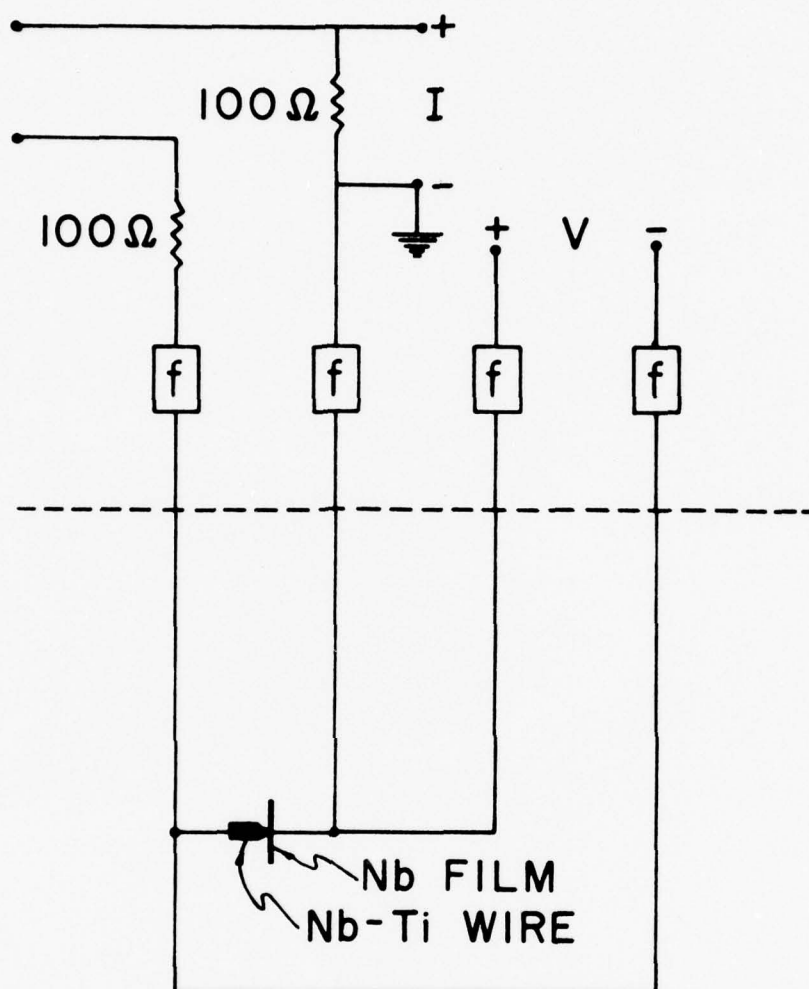
Block Diagram of the Biasing Circuit

according to the circuits described in Longacre's paper.³⁸ The junction VIC is displayed on an oscilloscope or plotted on an X-Y recorder by sweeping the junction current with a triangle wave generator. The attenuator network is shown in Fig. 15. The film side of the junction is grounded to the metal dewar which in turn is grounded to a common ground on the oscilloscope. To minimize rf pick up problems low pass LC filters with a cutoff frequency of 10 kHz are used in each of the leads that goes down to the junction.

Since the junction responsivity depends on the product of the maximum critical current I_c and the junction dynamic resistance R_D at the bias point, the highest responsivity is obtained by optimizing the product $I_c R_D$ on the junction VIC. Typical junction VICs of a 50 Å film point contact junction in the absence and presence of microwave radiation are shown in Fig. 16a and 16b respectively.

F. Video Detection Mode

In the video detection mode the junction is current biased on the junction VIC at a point where the dynamic resistance is high as shown in Fig. 17 and the incident microwave radiation is chopped or square wave modulated at a convenient frequency. The resulting voltage change at the chopping frequency is then detected with a standard phase sensitive detection system. A typical response curve for a 50 Å film point contact junction irradiated with 22GHz radiation is shown in Fig. 16.



f Erie Technological Products, Inc., EMI Suppression
Filters Series 1200-098; cutoff frequency 10 kHz.

FIGURE 15

Schematic Diagram of the Attenuator Network.
Those Components below the Dashed Line Are in
Liquid Helium.

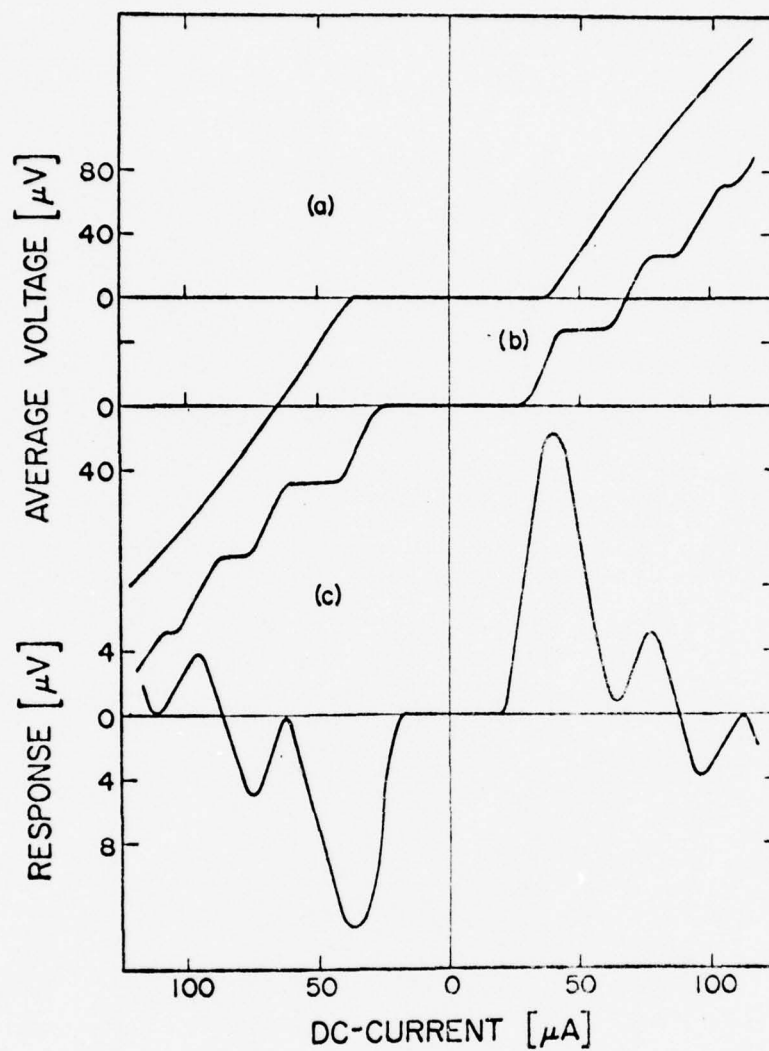


FIGURE 16

I-V Characteristics and Voltage Response Curve of a
50 Å Film Point Contact Junction:

- (a) I-V Characteristic in the Absence of Radiation;
- (b) I-V Characteristic in the Presence of 5mW 22GHz Radiation; and
- (c) Voltage Response Curve at 22GHz.

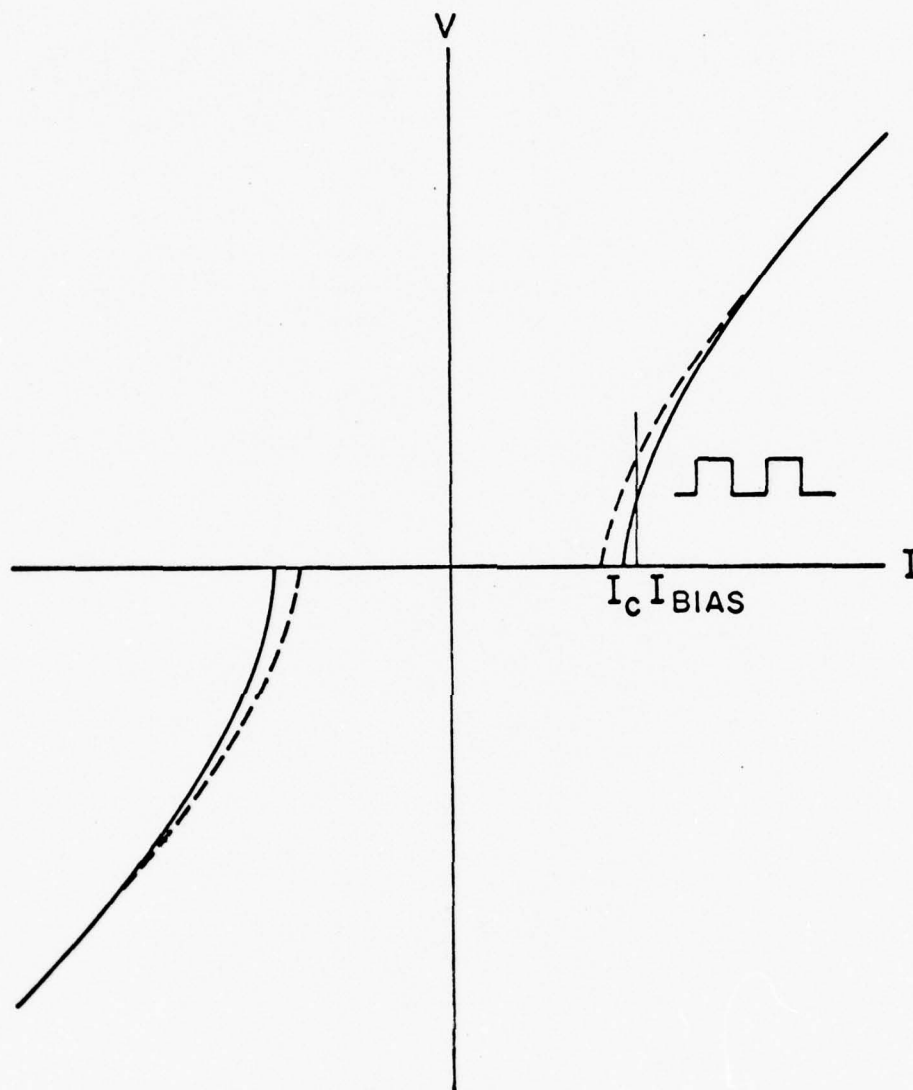


FIGURE 17

Schematic V-I Curve Showing how Applied Radiation Causes a Change in Zero Voltage Current which is Converted to a Voltage Output by Constant-Current External Bias.
 Dashed Curve is for Radiation on; Solid Curve for Radiation Off.

CHAPTER IV

EXPERIMENTAL RESULTS AND DISCUSSION

In this chapter experimental results on the responsivities of the junction in both the \vec{B} field and \vec{E} field coupling configurations are presented. Comparisons are made to the calculated responsivities and to other experiments.

A. \vec{B} Field Coupling Scheme

The responsivity of a thin-film-point-contact junction in the \vec{B} field coupling scheme is calculated in the following way:

From Eq. (76) of Chapter II the voltage response of the junction in the presence of low level monochromatic radiation is

$$\Delta \bar{V} = \frac{I_{co} R_D}{6} \left[\frac{\pi \lambda w B_0 e^{-t/\lambda}}{\Phi_0} \right]^2 \quad (76)$$

where the symbols are defined in Chapter II and will not be repeated here. If the microwave radiation is transmitted through a rectangular waveguide in the TE modes, the total power transmitted is related to the amplitude of the magnetic field by the following expression³⁹:

$$P_T = \frac{ab}{8} \sqrt{\frac{\mu}{\epsilon}} \frac{B_0^2}{\mu^2} \left(\frac{\lambda_0}{\lambda} \right)^2 \sqrt{1 - \left(\frac{\lambda}{\lambda_0} \right)^2} \quad (86)$$

where a and b (a greater than b) are the inner dimensions of the guide, μ and ϵ are the permeability and permittivity

respectively of the medium. In the medium under consideration which is either air or helium vapour $\mu = \mu_0$ and $\epsilon \approx \epsilon_0$, $\lambda_0 = 2a$ is the cut-off wavelength of the waveguide, and λ is the transmitted wavelength in the guide. For simplicity let us assume that the magnetic field threading the junction is the \vec{B} field in the TE modes. Writing B_0 in terms of P_T in Eq. (86) and substituting into Eq. (76) we get:

$$\Delta \bar{V} = \frac{I_{co} R_D}{6} \frac{P_T}{\frac{ab}{8\mu_0^2} \sqrt{\frac{\mu}{\epsilon}} \left(\frac{\lambda_0}{\lambda}\right)^2 \sqrt{1 - \left(\frac{\lambda}{\lambda_0}\right)^2}} \left[\frac{\pi \lambda w e^{-t/\lambda}}{\Phi_0} \right]^2 \quad (87)$$

Note that P_T , the total power transmitted is not the same as P , the incident power on the junction in the definition of the junction responsivity. Since the exact value of P is not easily measured we could only define our junction responsivity as:

$$R^* \equiv \frac{\Delta \bar{V}}{P_T} = \frac{I_{co} R_D}{6} \frac{1}{\frac{ab}{8\mu_0^2} \sqrt{\frac{\mu}{\epsilon}} \left(\frac{\lambda_0}{\lambda}\right)^2 \sqrt{1 - \left(\frac{\lambda}{\lambda_0}\right)^2}} \left[\frac{\pi \lambda w e^{-t/\lambda}}{\Phi_0} \right]^2 \quad (88)$$

In the above equation I_{co} , R_D , and w are the junction parameters and are easily measured. a , b and λ_0 are the waveguide parameters and depend on the size of the waveguide used. λ is measured by a wavemeter and should be very close to the free space wavelength. The remaining quantity is λ , the penetration depth of the film, which is not an easily measurable quantity. However, it is estimated in the following way.

As mentioned in Chapter II, λ depends on the mean free path, ℓ , of the sample. For a thin film sample with the thickness of the sample small compared to the other dimensions of the sample, ℓ is restricted by the thickness of the film. Also if ℓ is small compared to the range of coherence, the effective range of coherence is approximately equal to ℓ [Eq. (84), Chapter II]. For Nb, ξ_0 is $\approx 500 \text{ \AA}$. The film thickness studied ranges from 50 \AA to 500 \AA . In this range of film thickness ℓ is smaller than or equal to 500 \AA . Hence, to a first order approximation ξ is approximately equal to ℓ and λ is given as:

$$\lambda = \lambda_b \sqrt{\frac{\xi_0}{\xi(\ell)}} \approx \lambda_b \sqrt{\frac{\xi_0}{\ell}} \quad (89)$$

where λ_b for Nb is equal to 480 \AA at 4.2°K .

The estimated values for λ are listed in Table III. The mean free paths are essentially the same as the film thicknesses in the range considered. An oxide thickness of about 10 \AA grown on top of the sample further limits the mean free path, which becomes important for very thin films. This is taken into account for the three thinnest films considered.

A plot of the estimated penetration depths versus film thicknesses is shown in Fig. 18. The essential features are that λ is three to four times larger than that of the bulk value for a 50 \AA film and λ approaches λ_b for 500 \AA or thicker films.

TABLE III

CALCULATED PENETRATION DEPTHS

Film Thickness $t, (\text{\AA})$	Mean Free Path $\ell, (\text{\AA})$	Penetration Depth $\lambda, (\text{\AA})$
50	40	1700
100	90	1130
200	190	780
300	300	620
400	400	540
500	500	480

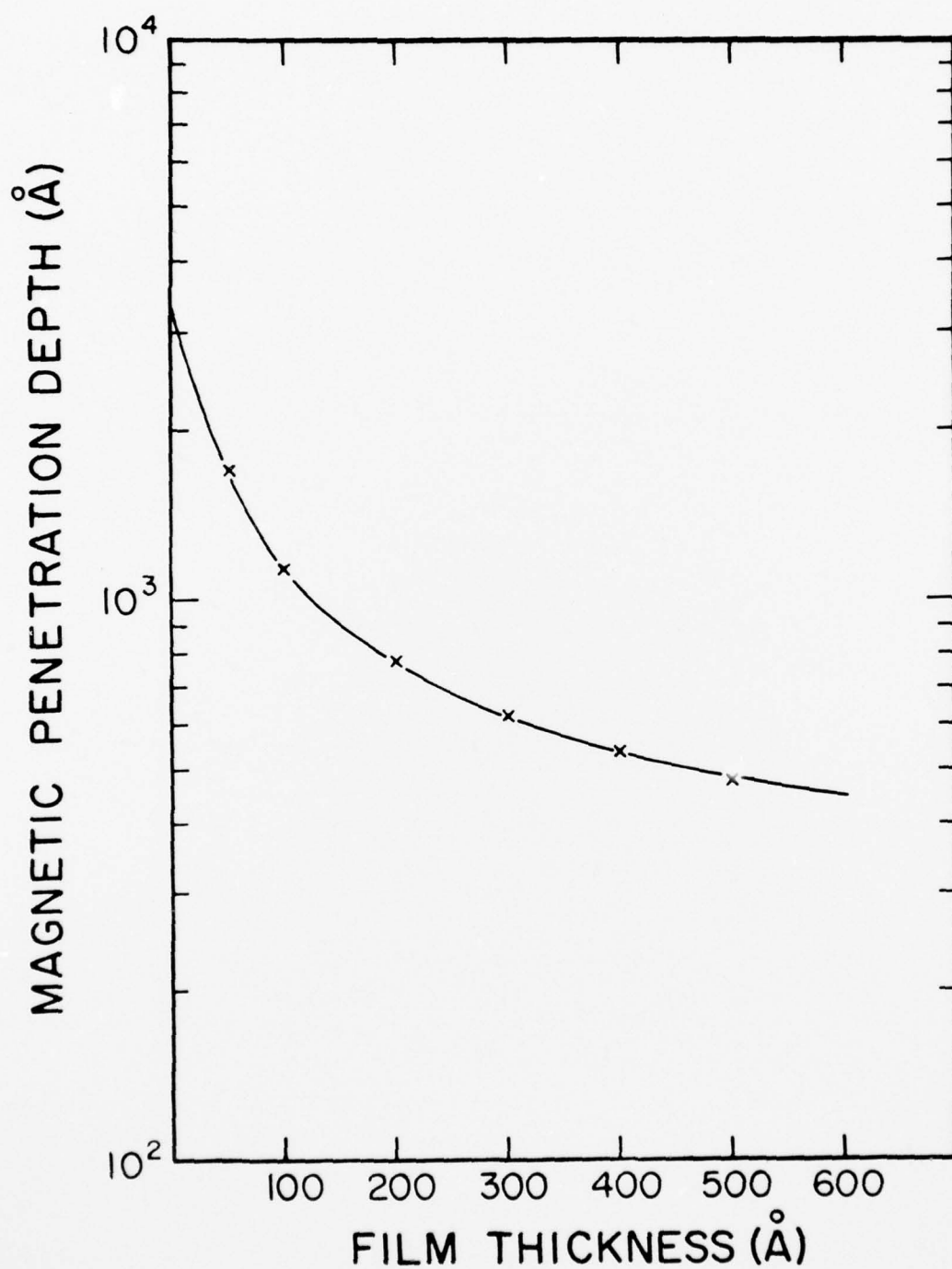


FIGURE 18

Plot of Penetration Depth Versus Film Thickness

In the present experiment a K-band waveguide is used for all the frequencies from 22GHz to 105GHz. The waveguide parameters are: $a = 1.07$ cm, $b = .432$ cm and $\lambda_0 = 2.14$ cm, which corresponds to a cut-off frequency of 14.1GHz.

The junction parameters (I_{co} , R_D , and w) vary from junction to junction because no two junctions are identically the same. Even during the same run the junction parameters are changed to obtain the optimum responsivity by varying the IV characteristics of the junction. The average values for I_{co} and R_D are respectively $200 \mu A$ and 10^4 ohms for junctions with high responsivities. The average value of w after the run is about $8 \times 10^{-5} m$ because the tip of the point is usually flattened by the Nb film on the sapphire substrate.

Using the average typical values for the junction parameters and the estimated penetration depths from Table III, the junction responsivities as a function of frequency and film thickness are calculated using Eq. (88). The calculated and measured responsivities are shown in Table IV. The average measured responsivity is the combined average of all the runs with a junction of the same thickness. There are no data for 66GHz and 105GHz for a junction with a 100 \AA or thicker film because the mm wave powers generated by the harmonic generators are not powerful enough to produce a detectable change in the junction VIC.

Plots of junction responsivity versus film thickness are shown in Fig. 19 and Fig. 20 for 22GHz and 35 GHz respectively. The solid curves are the calculated responsivity curve, the open

TABLE IV

RESPONSIVITY VS. FREQUENCY FOR VARIOUS POINT
CONTACT CONFIGURATIONS

Responsivity* V/W	22GHz	35GHz	66GHz	105GHz
\vec{B} field coupling 50 Ω Nb film and Nb-Ti point	5.1×10^{-2} (6×10^{-2})	1.7×10^{-2} (2.5×10^{-2})	4.5×10^{-3} (7.5×10^{-3})	1.7×10^{-3} (3×10^{-3})
\vec{B} field coupling 100 Ω Nb film and Nb-Ti point	2.0×10^{-2} (2×10^{-2})	6.4×10^{-3} (7×10^{-3})	1.7×10^{-3}	0.7×10^{-3}
\vec{B} field coupling 200 Ω Nb film and Nb-Ti point	0.7×10^{-2} (8×10^{-3})	2.2×10^{-3} (2.3×10^{-3})	5.9×10^{-4}	2.3×10^{-4}
\vec{B} field coupling 500 Ω Nb film and Nb-Ti point	5.4×10^{-4} (5×10^{-4})	1.8×10^{-4} (2.5×10^{-4})	4.7×10^{-5}	1.9×10^{-5}
** \vec{E} field coupling Nb-Ti sheet and Nb-Ti point	1.5×10^6 (3.6×10^5)	4.4×10^5 (6×10^4)	1.35×10^5 (1.5×10^5)	3.4×10^4 (6.8×10^4)
** \vec{E} field coupling Nb-Ti sheet and Nb pointed post	1.5×10^6 (4.3×10^5)	4.4×10^5 (8×10^4)	1.35×10^5 (1.6×10^5)	3.4×10^4 (5.1×10^4)
** \vec{E} field coupling 50 Ω Nb film and Nb-Ti point	1.5×10^6 (9×10^4)	4.4×10^5 (4×10^4)	1.35×10^5 (5.4×10^4)	3.4×10^4 (3.3×10^4)

* Responsivities in parentheses are average measured responsivity.

** The coupling is maximized only to 22 and 66GHz.

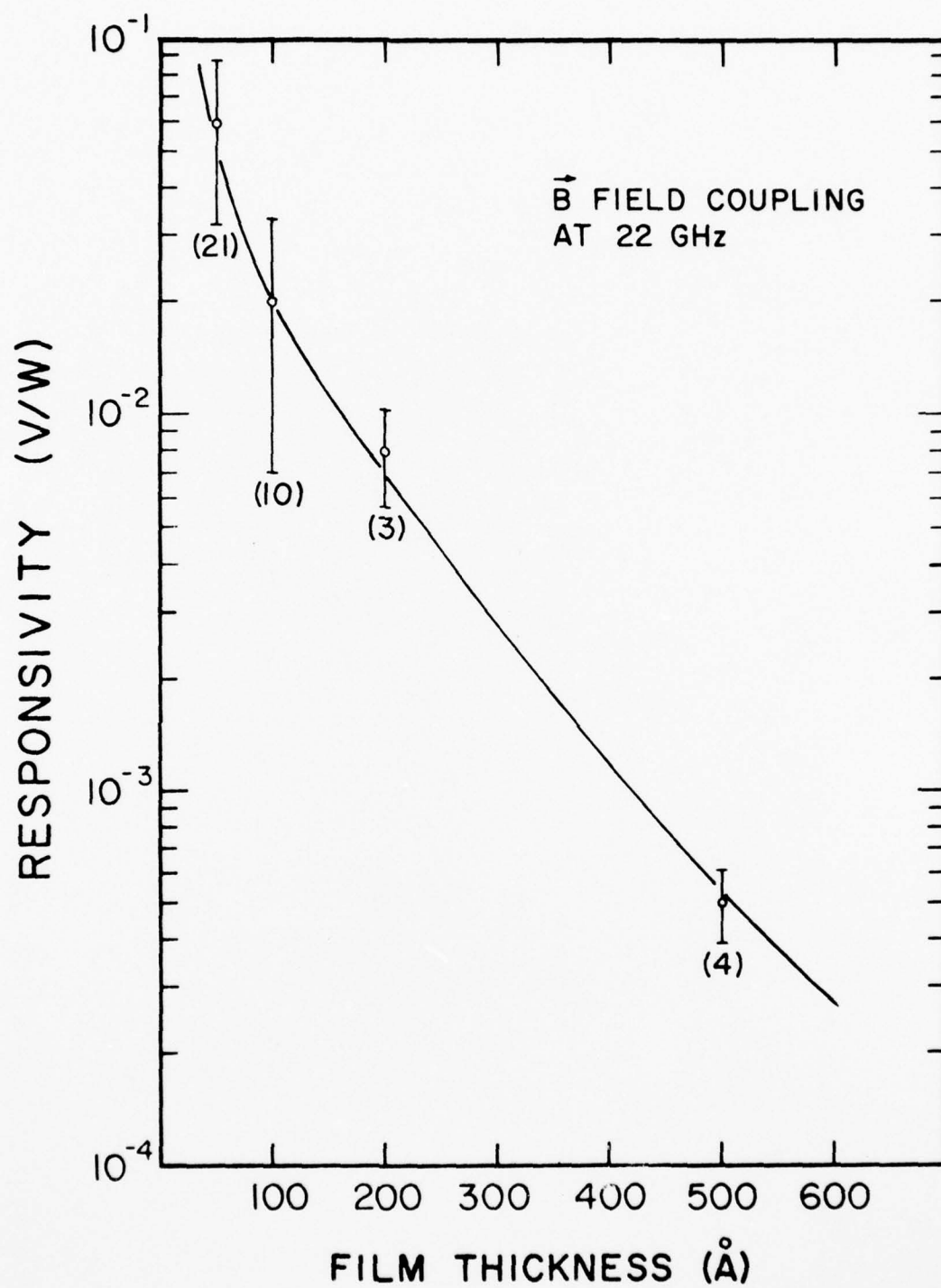


FIGURE 19

Plot of Junction Responsivity at 22GHz Versus Film Thickness

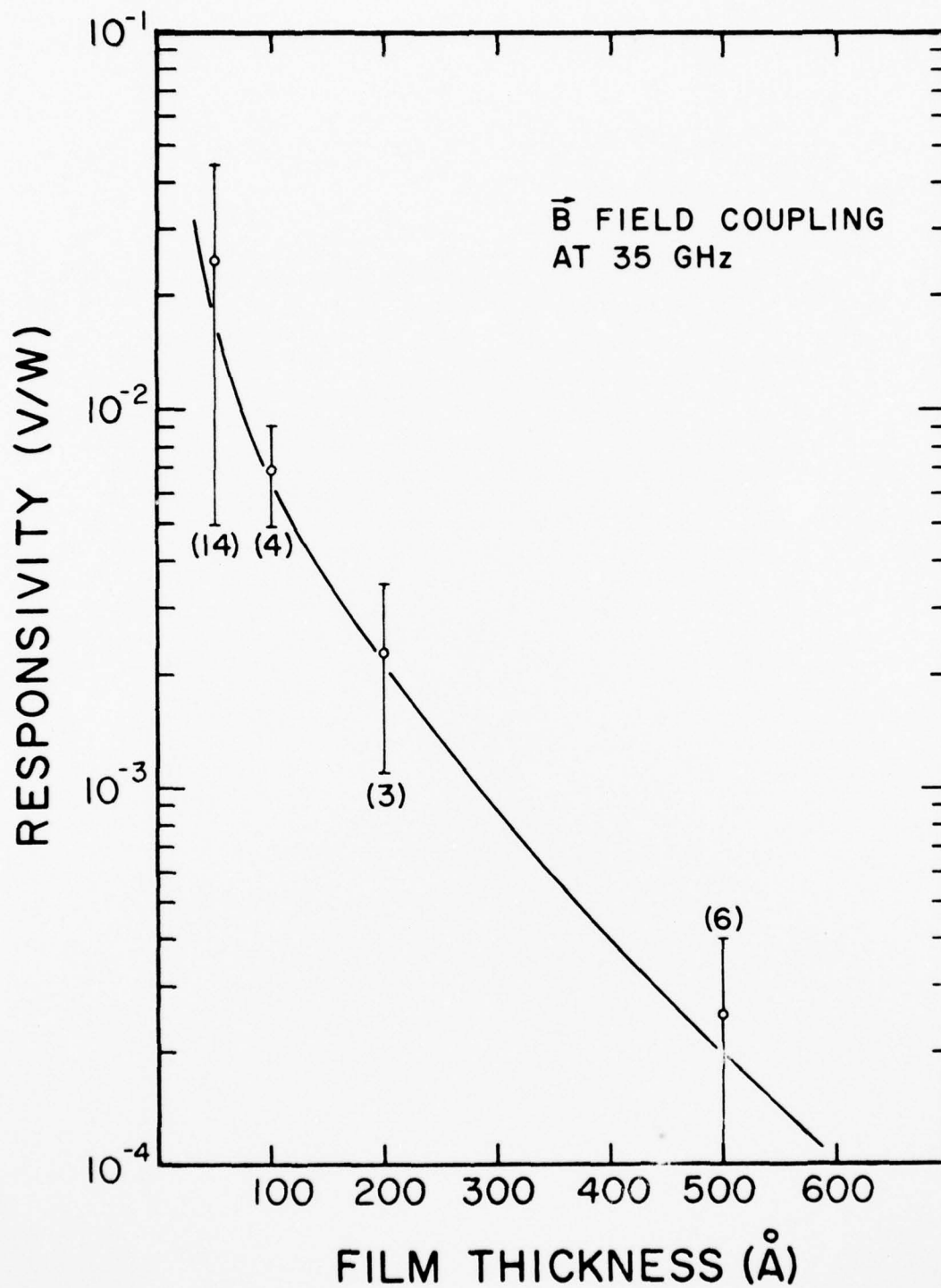


FIGURE 20

Plot of Junction Responsivity at 35GHz Versus Film Thickness

circles are the average measured responsivities and the bars correspond to one standard deviation. The number in parenthesis represents the number of individual IV characteristics used in the calculation of the mean and standard deviation. The measured responsivity agrees quite well with the calculated one.

B. \vec{E} Field Coupling Scheme

In this coupling configuration shown in Fig. 21 the point contact junction is put across a waveguide with its axis lying along the lines of maximum \vec{E} field. The voltage induced across the junction is:

$$V_1 = E_0 d \quad (90)$$

where E_0 is the amplitude of the \vec{E} field at the junction and d is an effective junction thickness of the order of twice the penetration depth of the superconductor forming the junction.

The responsivity of the junction in this coupling scheme is calculated in the following way:

The total transmitted power through a lossless rectangular waveguide is related to the amplitude of the electric field of the microwave radiation in the TM modes by the following expression³⁹

$$P_T = \frac{ab}{8} \sqrt{\frac{\epsilon}{\mu}} \left(\frac{\lambda_0}{\lambda} \right)^2 \sqrt{1 - \left(\frac{\lambda}{\lambda_0} \right)^2} E_0^2 \quad (91)$$

where the symbols have the same definitions as in Eq. (86).

Eliminating E_0 in Eqs. (90) and (91) and substituting the resulting

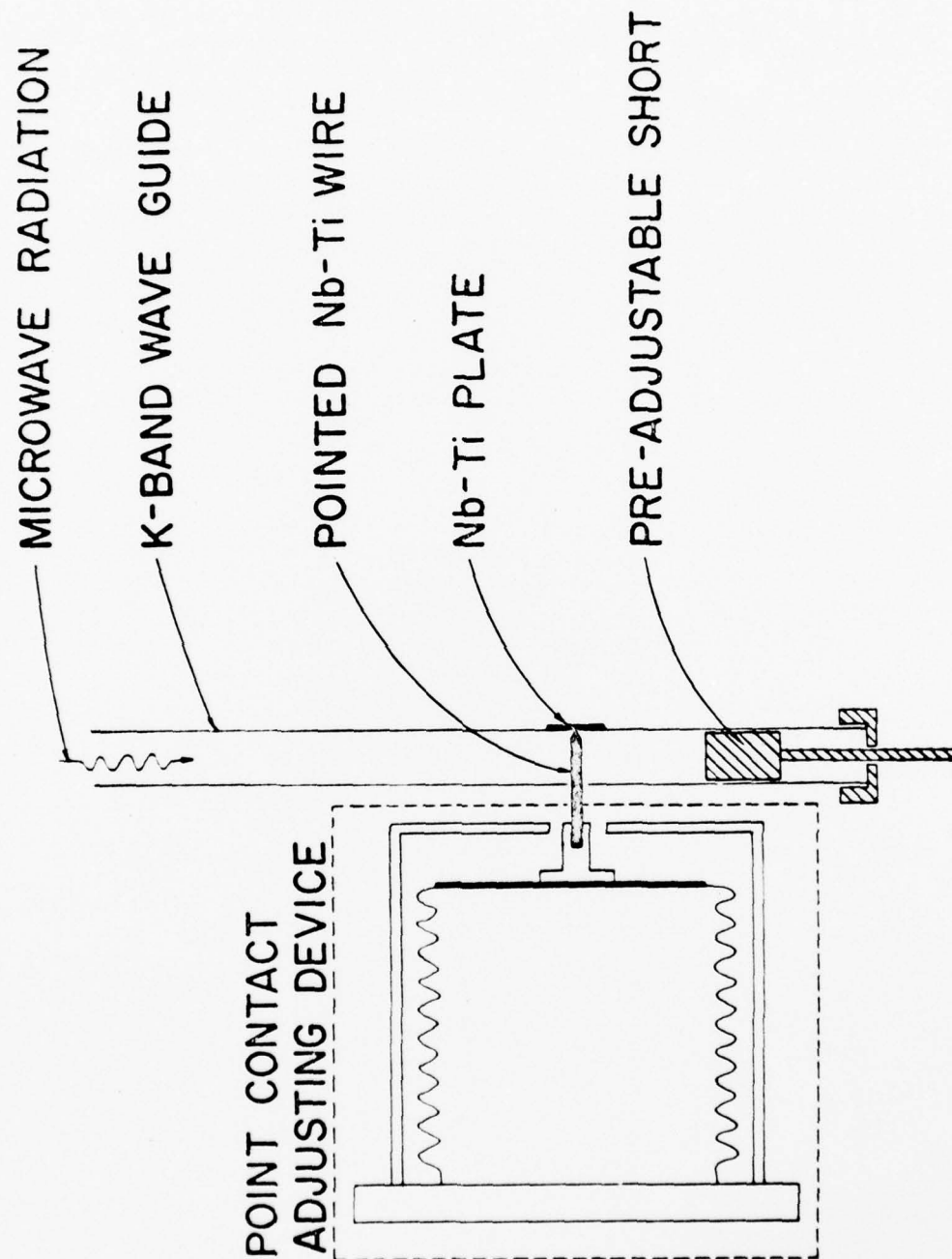


FIGURE 21

Schematic Drawing of the \vec{E} Field Coupling Scheme

equation for V_1 in Eq. (69) in Chapter II for the voltage response of the junction in this coupling scheme, we obtain:

$$\Delta \bar{V} = \frac{I_{co} R_D d^2 P_T}{\frac{ab}{8} \sqrt{\frac{\epsilon}{\mu}} \left(\frac{\lambda_0}{\lambda}\right)^2 \sqrt{1 - \left(\frac{\lambda}{\lambda_0}\right)^2}} \left(\frac{e}{\hbar \omega}\right)^2 \quad (92)$$

But the power input to the junction is only a small fraction of P_T due to impedance mismatch between the waveguide and the point contact junction. Substituting $P = fP_T$ in Eq. (92) we obtain the junction responsivity as:

$$R \equiv \frac{\Delta \bar{V}}{P} = \frac{I_{co} R_D d^2 / f}{\frac{ab}{8} \sqrt{\frac{\epsilon}{\mu}} \left(\frac{\lambda_0}{\lambda}\right)^2 \sqrt{1 - \left(\frac{\lambda}{\lambda_0}\right)^2}} \left(\frac{e}{\hbar \omega}\right)^2 \quad (93)$$

The fraction of power absorbed by the junction, f , is estimated by the equivalent circuit of the junction as shown in Fig. 6. When there is a mismatch between the characteristic impedance of the waveguide and the load impedance of the junction, the fraction of maximum possible power absorbed by the circuit from the source is given by:⁴⁰

$$f = \frac{4R_L R_O}{|R_O + R_L + iX_L|^2} \quad (94)$$

where R_O is the characteristic impedance of the guide and $Z_L = R_L + iX_L$ is the load impedance of the junction.

The main contribution to the inductance, L , of the junction is the length of the pointed wire across the waveguide. The inductance of a straight wire of diameter .64 mm and length 1 mm

is 2.2×10^{-10} Henry. The capacitance of the junction is $C = \frac{\epsilon A}{d}$, where $\epsilon = 20 \epsilon_0$ for Nb_2O_5 at 10^{10} GHz, d is the oxide thickness of the junction and $A = \pi r^2$ is the area of the junction. The estimated dimensions of the junction are $r = 10^{-5}$ m and $d = 20 \text{ \AA}$ which give a junction capacitance of 28 pF. Note that the junction width is smaller than the previous case because the point does not have to push as hard on a superconductor as it has to on a Nb film on a sapphire substrate to form a junction. The junction resistance in the normal state is about 10 ohms. Using the above values for L , C , and R_n and the characteristic impedance of a K-band waveguide, the fraction, f , for a particular frequency is calculated.

The estimated value for d in Eq. (93) is 1000 \AA which is about twice the penetration depth of Nb at 4.2°K. Typical values of I_{co} and R_D are 200 μA and 10^4 ohms for our junctions. All the experiments are performed with the junction inside a K-band waveguide. The frequency range studied is from 22GHz to 105GHz. The waveguide is terminated with an adjustable short which is set at a distance of a $1/4$ free space wavelength of 22GHz from the junction. This distance is set before the run and cannot be adjusted during the run. Hence, the \vec{E} field at the junction is approximately maximized only to 22 and 66GHz but not to 35 and 105GHz.

The calculated responsivities using Eq. (93) and the measured responsivities for three different junctions are listed in the lower half of Table IV. The estimated error for the 22GHz

and 35GHz measurements is $\pm 10\%$ due to uncertainties in the rated power outputs of the sources. The estimated error for the 66GHz and 105GHz measurements is $\pm 20\%$ due to the additional uncertainties in the power outputs of the harmonic generators.

The measured values of responsivity are generally lower than the predicted values especially for 35GHz. This is due to the fact that the junction configuration is designed for wide band detection and is not tuned to any particular frequency. The $1/\omega^2$ dependence predicted in Eq. (93) is approximately followed by all the junctions. The low responsivities for the 50 Å film junction is due to a lower critical current density in the film which reduces I_{co} of the junction.

Our measured responsivities although slightly lower are comparable to the reported responsivities in the experiments of Kanter and Vernon⁴ and Divin and Nad'.⁵

CHAPTER V

CONCLUSION AND FUTURE EXPERIMENTS

Our experiments show that the responsivity in the \vec{B} field coupling scheme is low compared to that in the \vec{E} field coupling scheme. The reason for this is that in the \vec{B} field coupling scheme described in this experiment the radiation \vec{E} field is not strongly coupled to the junction. There are at least two ways to improve on the responsivity of the \vec{B} field coupling scheme. One involves the use of a double point contact junction to increase the magnetic flux threading the junctions and the other involves the use of a Fabry-Perot resonant cavity to increase the field intensity at the junction. These two methods are discussed below.

The first method is to make a double point contact junction on the film instead of just a single point contact as in the previous case (Fig. 22). If the two Josephson junctions are identical and are connected in parallel the maximum supercurrent flowing through the two junctions is given by the formula¹³

$$I_{\max} = 2I_{\text{co}} \left| \frac{\sin(\pi \Phi_j / \Phi_0)}{\pi \Phi_j / \Phi_0} \right| \left| \cos \frac{\pi \Phi_{\text{int}}}{\Phi_0} \right| \quad (95)$$

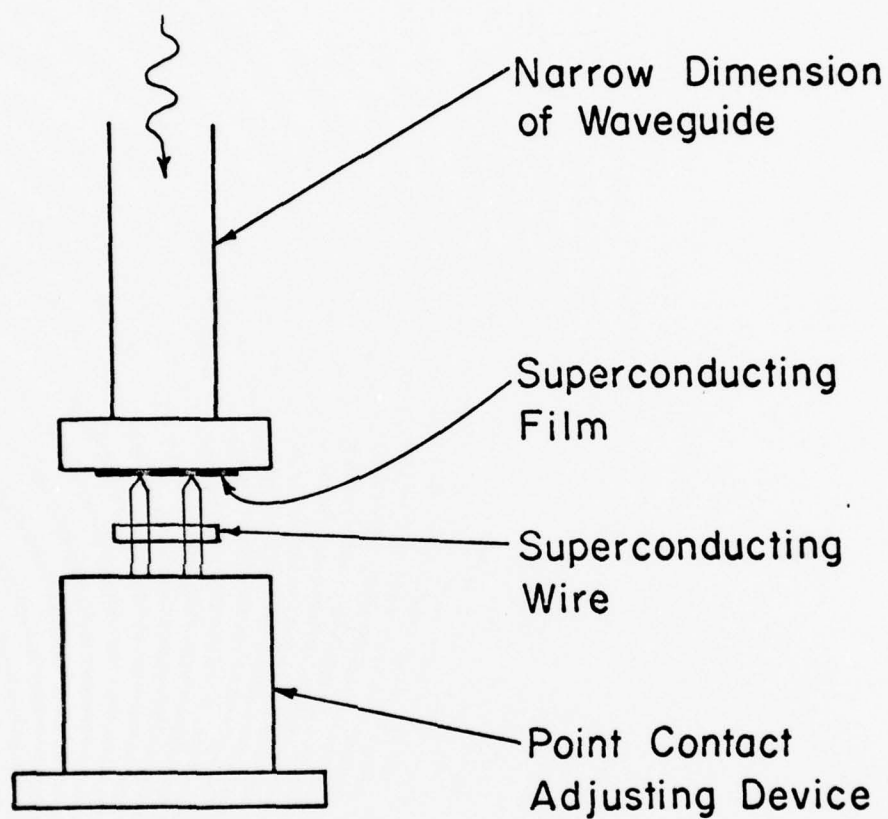


FIGURE 22

Schematic Drawing of a Double Point Contact Junction
in the \vec{B} Field Coupling Scheme

where I_{co} is the maximum critical current of a single junction,

Φ_j is the magnetic flux enclosed by each junction and Φ_{int} is the flux enclosed in the loop formed by the two junctions. The sine term is the modulation of I_{co} due to the magnetic flux threading the individual junctions and the cosine term is the modulation due to the magnetic flux threading the loop of the junctions. For radiation coming through the back of the film

$\Phi_j = \lambda w B_0 e^{-t/\lambda}$ and $\Phi_{int} = \lambda L B_0 e^{-t/\lambda}$, where w and L are the width and separation of the junctions respectively. Since L is usually much larger than w of the individual junctions, the cosine term in Eq. (95) varies much faster than the sine term.

For low level radiation such that $\Phi_j \ll \Phi_{int} \ll \Phi_0$, a flux quantum, we only need to concentrate on the cosine term. Following a similar derivation leading to Eq. (76) for a single point contact, the responsivity of a double point contact is obtained as:

$$R \approx \frac{I_{co} R_D}{P} \left[\frac{\pi \lambda L B_0 e^{-t/\lambda}}{\Phi_0} \right]^2 \quad (96)$$

Comparing Eq. (96) with Eq. (76) we see that R is increased by a factor of $(L/w)^2$ for a double point contact. Note that L is limited by the wavelength of the incident radiation. Further increase in L results in a reduction of Φ_{int} because of cancellation of the fields.

Preliminary experiments with a 50 Å film double point contact junction with a separation of about 1 mm show an increase

in R of two orders of magnitude at 22GHz from a single point contact in the \vec{B} field coupling configuration. $(L/w)^2$ is about 150 in this case. One of the difficulties in this experiment is to try to make two junctions simultaneously with one point contact adjusting mechanism.

Another method is to use a semiconfocal type Fabry-Perot resonator (Fig. 23) to increase the \vec{B} field at the junction. The resonator is believed to be most suitable for operation in the millimeter wave region. It consists of two circular reflectors between which standing wave TEM modes are maintained. One reflector is a concave spherical mirror through which is passed a millimeter waveguide. Power is coupled into the cavity through the waveguide. The other reflector is a planar surface formed by a film of a superconductor. Contact is made to the center of the film where the fields are high. To facilitate coupling of power out of the cavity and into the junction a small area of the film at the junction is made thin compared to the penetration depth of the film. Means have to be provided for adjusting the distance between the two reflectors so that the cavity can be tuned to a broad range of frequencies. While this method of coupling will enhance the magnetic field at the junction and therefore the responsivity, the fields at the junction are not easily calculated.

The estimated coupling coefficients for the \vec{E} field in the \vec{B} field and \vec{E} field coupling schemes studied are of the order of 10^{-5} and 10^{-3} , respectively. This accounts for the low

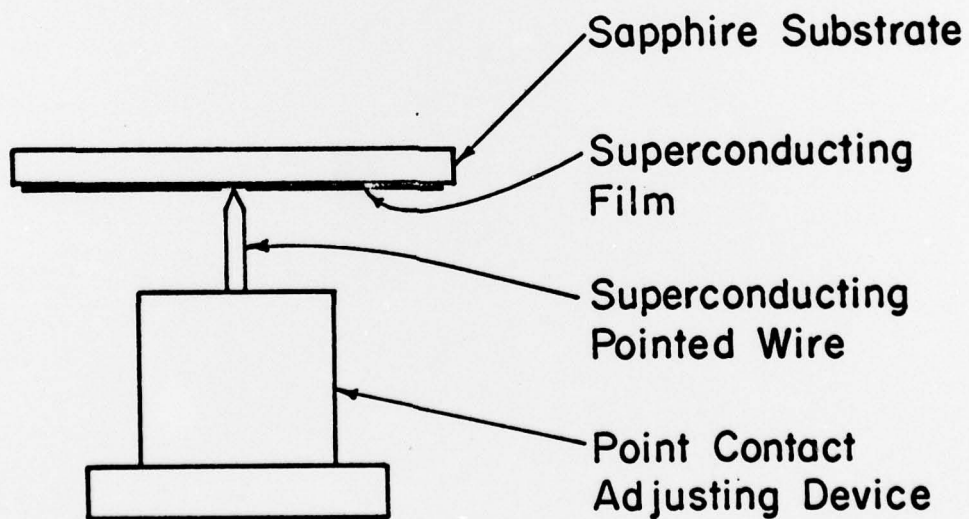
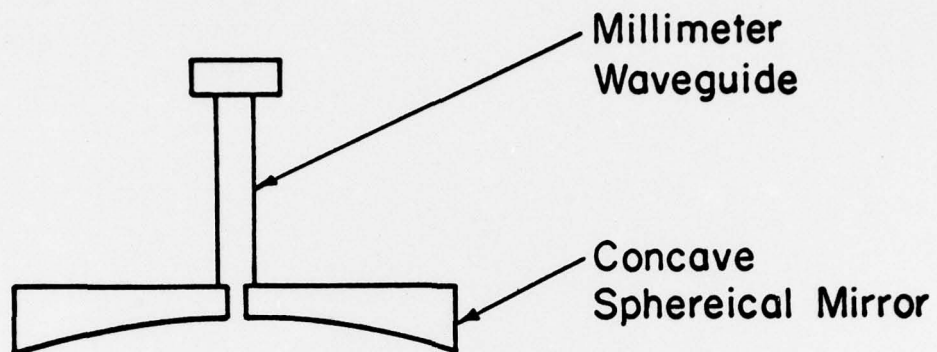


FIGURE 23

Schematic Diagram of a Fabry-Perot Resonator Coupled
to a Point Contact Josephson Junction

responsivities in our experiments. Our conclusion is that for successful use of simple Josephson junction detectors in the millimeter and submillimeter region it is probably crucial not only to impedance match the junction to the radiation source but also to make them a part of a resonant structure.

REFERENCES

1. B. D. Josephson, Physics Letters 1, 251 (1962).
2. C. C. Grimes, P. L. Richards and S. Shapiro, Phys. Rev. Letters 8, 431 (1966); J. Appl. Phys. 39, 3905 (1968).
3. P.L. Richards and S. A. Sterling, Appl. Phys. Letters 14, 394 (1969).
4. H. Kanter and F. L. Vernon, Jr., J. Appl. Phys. 43, 3174 (1972).
5. Yu. Ya. Davin and F. Ya. Nad', Radio Eng. Electron. Phys. 18, 642 (1973).
6. F. London, Superfluids, vol. I (John Wiley, New York, 1950); Phys. Rev. 74, 562 (1948).
7. V. L. Ginzburg and L. D. Landau, Zh. Eksperim. i Teor. Fiz. 12, 1064 (1950); English Transl.: Men of Physics, L. D. Landau, vol. 1, ed. by D. ter Haar (Progamon Press, London, 1965) p. 138.
8. C. J. Gorter and H. B. G. Casimir, Physica 1, 306 (1934); Phys. Z. 35, 963 (1934); Z. techn. Phys. 15, 539 (1934).
9. L. N. Cooper, Phys. Rev. 104, 1189 (1956); J. Bardeen, L. N. Cooper and J. R. Schrieffer, Phys. Rev. 108, 1175 (1957).
10. P. W. Anderson in: Progress in Low Temperature Physics 5, ed. C. J. Gorter (North-Holland Publ. Co., Amsterdam, 1967) p. 32.
11. B. S. Deaver and W. M. Fairbank, Phys. Rev. Lett. 7, 43 (1961).
12. M. Doll and M. Nöbauer, Phys. Rev. Lett. 7, 51 (1961); Z. Physik 169, 526 (1962).
13. L. Solymar, Superconductive Tunneling and Applications, (Wiley-Interscience, New York, 1972) p. 146.
14. R. P. Feynman, R. B. Leighton and M. Sands, The Feynman Lectures on Physics, vol. III, chap. 21, (Addison-Wesley, Reading, Massachusetts, 1965).

15. A. Th. A. M. de Waele and R. de Bruyn Ouboter, *Physica* 41, 225 (1969); see also R. de Bruyn Ouboter and A. Th. A. M. de Waele in *Progress in Low Temp. Phys.* vol. VI, ch. 6, ed. C. J. Gorter (1970).
16. V. Ambegaokar and A. Baratoff, *Phys. Rev. Lett.* 10, 486 (1963); Erratum, *Phys. Rev. Letts.* 11, 104 (1963).
17. P. W. Anderson and J. M. Rowell, *Phys. Rev. Letts.* 10, 230 (1963).
18. I. S. Gradshteyn and I. M. Ryzhik, 'Table of Integrals, Series and Products', (Academic Press, New York, 1965).
19. S. Shapiro, *Phys. Rev. Letts.* 11, 80 (1963).
20. S. Shapiro, A. R. Janus and S. Holly, *Rev. Mod. Phys.* 36, 223 (1964).
21. W. C. Stewart, *Appl. Phys. Lett.* 12, 277 (1968).
22. D. E. McCumber, *J. Appl. Phys.* 39, 297, 2503, 3113 (1968).
23. D. G. McDonald, A. S. Risley, J. D. Cuppa, J. M. Everson, and J. R. Ashley, *Appl. Phys. Lett.* 20, 296 (1972).
24. A. B. Pippard, *Proc. Roy. Soc.* A216, 547 (1953).
25. J. Bardeen, *Theory of Superconductivity*, *Handbuch der Physik*, Vol. XV, S. Flügge, ed.; Berlin, Springer (1956).
26. E. A. Lynton, *Superconductivity* (Methuen & Co., Ltd., London, 1969) p. 47.
27. B. W. Maxfield and W. L. McLean, *Phys. Rev.* 139, A1515 (1965).
28. A. Contaldo, *Rev. Sci. Instrum.* 38, 1543 (1967).
29. C. A. Neugebauer and R. A. Ekvall, *J. of Appl. Phys.* 35, 547 (1964).
30. H. C. Theuerer and J. J. Hauser, *J. of Appl. Phys.* 35, 554 (1964).
31. H. London and R. G. Clarke, *Rev. of Mod. Phys.* 36, 320 (1964).
32. J. J. Hauser and H. C. Theuerer, *Phys. Rev.* 134, A198 (1964).
33. R. P. Huebener, R. T. Kampeirith, R. L. Martin, T. W. Barbee, Jr., and R. B. Zubeck, *J. of Low Temp. Phys.* 19, 247 (1975).

34. Y. Saito and T. Anayama, J. of Low Temp. Phys. 21, 169 (1975).
35. W. C. King and W. Gordy, Phys. Rev. 93, 407 (1954).
36. W. Gordy, Pure and Appl. Chem. 11, 403 (1965).
37. R. S. Ohl, P. P. Budenstein, and C. A. Burrus, Rev. of Sci. Instrum. 30, 765 (1959).
38. A. Longacre, Jr., Rev. Sci. Instrum. 41, 448 (1970).
39. A. B. Bronwell and R. E. Beam, Theory and Application of Microwaves, McGraw-Hill, New York (1947) p. 354.
40. A. B. Bronwell and R. E. Beam, Theory and Application of Microwaves, McGraw-Hill, New York (1947) p. 189.
41. S. I. Bondarenko, I. M. Dmitrienko and T. P. Narbut, Sov. Phys. Solid State 14, 295 (1972).

VITA

PII Redacted

Chi-Kong So [REDACTED], where he received elementary and high school education. In 1966 he graduated from Pui Ching High School. In the same year he was awarded a government bursary to study at the Chinese University of Hong Kong. He received his B.S. degree in physics in 1970. In September 1970, he came to the United States for post-graduate studies and received his M.S. degree in August, 1972 from the Louisiana State University. He is now a candidate for the degree of Doctor of Philosophy in the Department of Physics and Astronomy at the Louisiana State University.

He is a member of the American Physical Society.